Computer Methods in Applied Mechanics and Engineering 449 (2026) 118553

Contents lists available at ScienceDirect

Comput. Methods Appl. Mech. Engrg.

journal homepage: www.elsevier.com/locate/cma

# A novel virtual element formulation for geometrically exact three-dimensional beams

Pierfrancesco Gaziano [a,*], Michele Marino [a], Giuseppe Vairo [a,b], Peter Wriggers [c]

[a] Multiscale and Multiphysics Mechanics Group (M2M), Department of Civil Engineering and Computer Science Engineering, University of Rome "Tor Vergata", Via del Politecnico 1, Rome, 00133, Italy
[b] Department of Mechanical Engineering, University of Brasília, Campus Darcy Ribeiro, Asa Norte, Brasília, 70910-900, DF, Brazil
[c] Institute for Continuum Mechanics, Leibniz Universität Hannover, Gebäude 8142, An d. Universität 1, Garbsen, 30823, Germany

ARTICLE INFO

*Keywords:*
Virtual element method
Geometrically exact beam models
3D finite rotations
Large deflections
Locking-free formulations
High-order beam elements

ABSTRACT

Discretization techniques for large-displacement analyses of shear-deformable 3D beams should ideally introduce a minimal number of unknowns with a clear physical interpretation and that should possibly be approximated through polynomials of generic degree. Moreover, numerical formulations should be objective, locking-free and singularity-free for arbitrarily large rotations. In this context, the Virtual Element (VE) method offers significant potential that remains to be fully explored. In this work, we propose a novel VE formulation that enables the construction of new nonlinear 3D beam elements of arbitrary polynomial interpolation order. The proposed formulation introduces displacements and rotations at the element endpoints as the only unknowns, even in the case of high-order interpolation functions, as the additional internal degrees of freedom are statically condensed at the element level. The consistency, robustness, and accuracy of this new formulation are assessed through a series of well-established benchmark tests. Numerical results confirm that the developed 3D beam virtual elements are computationally efficient, locking-free, and highly accurate, particularly when high-order ansatz functions are used.

## 1. Introduction

Beam- or rod-like components represent essential constituents of many engineering structures in applications such as aerospace, civil infrastructure, marine engineering, flexible multibody systems, as well as biomechanics [1–5]. In many instances, specific application requirements call for structural systems that exhibit low mass and high flexibility. These highly slender beam-like structural components, inherently lightweight yet capable of bearing significant loads, are massively exploited to minimize mass and material usage. Examples include wind turbines [3,6], deployable space structures [7,8], and smart materials and structures for energy absorption [9,10].

The same high slenderness also endows these structural elements with a very pronounced flexibility. As a consequence, under typical operative loading conditions, beams often undergo large displacements and rotations while the associated strains remain small [11]. Such geometric nonlinearity may also give rise to complex structural responses involving instability phenomena (snap-through, snap-back, buckling, etc.) that classical small-displacement beam theories fail to capture. In this context, accurate prediction

* Corresponding author.
*E-mail address:* gaziano@ing.uniroma2.it (P. Gaziano).

https://doi.org/10.1016/j.cma.2025.118553
Received 19 June 2025; Received in revised form 29 September 2025; Accepted 3 November 2025

of displacements, rotations, and stress resultants is essential to ensure safety, reliability, and performance in the design of systems where slender rods serve as primary load-bearing or kinematic members.

A wide variety of analytical and numerical formulations has been developed over the past century to address these challenges. Among the different available three-dimensional models, geometrically exact beam formulations, based on the theory developed in 2D by Reissner [12,13] and subsequently refined and generalized by Simo [14,15] in the 3D case, have proven particularly effective compared to other strategies, such as the methods of absolute nodal coordinates [16] or solid beam elements [17]. By rigorously accounting for finite rotations and large deformations, these theories provide a unified framework capable of representing the full geometrically nonlinear response of shear-deformable beams. Nevertheless, effective modeling of structures involving geometrically exact 3D beams remains nontrivial because arbitrarily large 3D rotations require special treatment, as they are described by orthogonal transformations in the Euclidean space and therefore constitute a non-commutative (Lie) group [15,18]. Numerous computational strategies, each with its own trade-offs in terms of complexity, accuracy, and robustness, have been developed to tackle the problem of 3D finite rotations, including corotational approaches [19,20], formulations based on quaternions [15,21], and even rotation-free discrete frameworks [22,23]. Among the different ways of parameterizing 3D rotations, one of the preferable approaches seems to be the use of the Euler rotation vector [24,25], since it requires only three independent parameters, each with a clear physical meaning, which also facilitates the enforcement of boundary conditions. Moreover, a direct interpolation of the Euler rotation vector ensures that the updating procedure becomes additive, leading to path-independent solutions under conservative loading conditions [21,26].

Regardless of the parameterization of finite rotations, desirable discretization techniques for shear-deformable 3D beams should employ a small number of physically meaningful unknowns and lead to objective and locking-free solutions [11]. The phenomenon of locking is related to a mismatch in the order of polynomial interpolation for deflections and rotations, since the resulting strain measures depend both on rotations and on the first derivatives of the displacements [27]. Locking can be overcome using a variety of approaches [2,28], such as reduced integration [29], mixed interpolations [30] and discrete shear gap elements [31] in the context of finite element (FE) technologies. An attractive alternative to FE methodologies is to adopt formulations based on isogeometric analysis (IGA) [11,32]. Specifically, IGA formulations based on collocation schemes were shown to possess additional advantages over the more conventional Galërkin approaches, like inherent locking-free behavior and reduced computational cost, even if a small price is paid in terms of accuracy [33–37].

In the framework of advanced modeling techniques for structural mechanics problems, the virtual element (VE) method has recently emerged as a valid and effective alternative to classical FE technologies or IGA. First introduced by Beirão da Veiga et al. [38,39], the VE methodology provides more flexible ways of discretizing geometries, such as the inclusion of mesh elements that have an arbitrary number of edges and/or can even be nonconvex. Interestingly, in some specific cases the VE method produces elements which are equivalent to the classical, well-known finite elements [27,40]. In this sense, the VE approach can be regarded as a generalization of the FE method. However, a key distinction between the two approaches lies in the construction of elements based on higher-order interpolation functions, which has proven particularly effective for one-dimensional geometries in the 2D case. Indeed, the VE approach enables a simple and systematic derivation of accurate, locking-free, and high-order beam elements, which can provide better approximations of the deflections and stress resultants within the elements [27,40]. The FE counterpart of these elements can be obtained only using specific formulations that incorporate special techniques to heal shear-locking (e.g., reduced integration, assumed natural strain, etc.) [28]. This may explain the reason why beam FE formulations based on higher-order ansatz functions are extremely rare in the literature. To the best of the authors' knowledge, only Moallemi-Oreh et al. partially addressed this aspect, even if restricting to a 2D case in the linear regime [41]. Conversely, the flexibility of the VE method gives major and unique advantages for building in an automatic and modular way numerical formulations for beam elements in a 2D setting. However, to date, no VE formulation has been developed for beams undergoing large deflections and finite rotations in a 3D context.

In this work, we propose a novel VE formulation for geometrically exact 3D beams based on the Simo-Reissner theory, extending the VE framework for the 2D Timoshenko beam developed by Wriggers [27]. This novel VE formulation introduces displacements and rotations at the element endpoints as the only nodal unknowns. This holds true even for higher-order ansatz spaces, where additional unknowns must be introduced. These are related to internal variables (not associated with any node) and can therefore be condensed out at the element level. Thus, the resulting virtual elements can be readily implemented in any FE software. The accuracy and locking-free performance of the proposed Simo-Reissner 3D virtual beam element have been assessed through a series of well-established benchmark numerical tests. The results confirm the effectiveness of the proposed VE framework for one-dimensional structures, even within a fully nonlinear three-dimensional setting.

## 2. Theoretical background for 3D beam theory

This section recalls some fundamental concepts of the theory of geometrically exact three-dimensional beams [14,15,42], also with the aim of introducing a consistent set of notation.

### 2.1. Kinematic description

As depicted in Fig. 1, the reference (or initial) configuration $\mathscr{B}_0$ of a generic beam is defined by a family $\mathscr{A}_0$ of cross sections whose centroids are connected by a piecewise smooth curve $\boldsymbol{r}_0(s) \in \mathbb{R}^3$, where $s \in [0, \ell]$ is the curvilinear abscissa and $\ell$ the initial beam length. This curve is referred to as the beam axis, or line of centroids. Each cross section $\mathcal{A}_0 = \mathcal{A}_0(s) \in \mathscr{A}_0$ is assumed to be a regular bounded domain contained in $\mathbb{R}^2$. The description of the beam reference configuration is completed by assigning a field of orthonormal right-handed triads $\{\boldsymbol{T}_1(s), \boldsymbol{T}_2(s), \boldsymbol{T}_3(s)\}$ attached to each cross section of the beam. In particular, $\boldsymbol{T}_1$ represents the unit

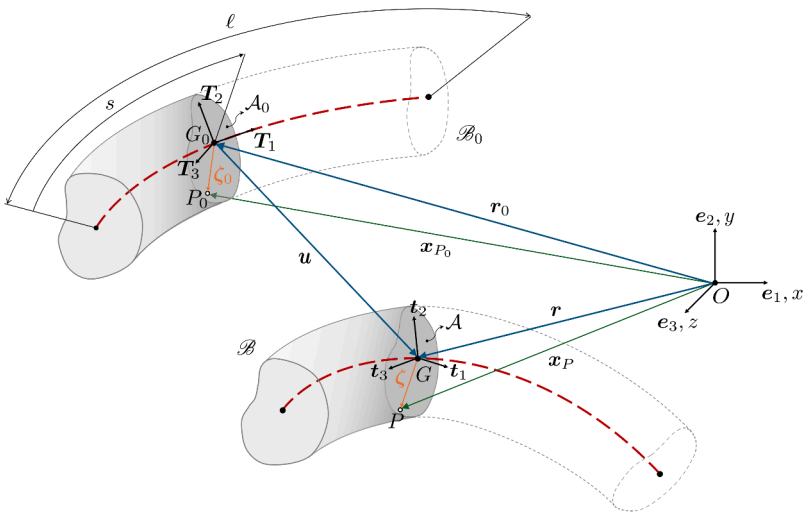


**Fig. 1.** Three-dimensional beam model. Problem description and notation.

vector tangent to the undeformed beam axis, while $\boldsymbol{T}_2$ and $\boldsymbol{T}_3$ are aligned with the principal axes of each cross section. Denoting by $\{\boldsymbol{e}_1, \boldsymbol{e}_2, \boldsymbol{e}_3\}$ a right-handed orthonormal base associated with a fixed Cartesian reference system $Oxyz$, the two-point tensorial field $\boldsymbol{\Lambda}_0 = \boldsymbol{\Lambda}_0(s)$ maps, for each $i \in \{1, 2, 3\}$, the fixed unit vector $\boldsymbol{e}_i$ to $\boldsymbol{T}_i$:

$$\boldsymbol{T}_i = \boldsymbol{\Lambda}_0\, \boldsymbol{e}_i \quad (i = 1, 2, 3) \quad \Rightarrow \quad \boldsymbol{\Lambda}_0 = \sum_{i=1}^{3} \boldsymbol{T}_i \otimes \boldsymbol{e}_i. \tag{1}$$

Since $\|\boldsymbol{e}_i\| = \|\boldsymbol{T}_i\| = 1$ for each $i = 1, 2, 3$ and both bases follow the same sign condition, $\boldsymbol{\Lambda}_0$ must be a proper orthogonal tensor, i.e., it belongs to the special orthogonal group SO(3):

$$\mathrm{SO}(3) = \{\mathbf{R} \,:\, \mathbb{R}^3 \mapsto \mathbb{R}^3 \mid \det(\mathbf{R}) = 1,\ \mathbf{R}\mathbf{R}^{\mathrm{T}} = \mathbf{R}^{\mathrm{T}}\mathbf{R} = \mathbf{I}\}, \tag{2}$$

with $\mathbf{I}$ being the second-order identity tensor.

Adopting the classical kinematic hypothesis that the cross sections remain plane and are subjected only to rigid motions, the deformed (or actual) configuration of the beam $\mathscr{B}$ is fully described by the current position of its axis and the current orientation of each cross section. Specifically, the centroid $G_0$ located at $\boldsymbol{r}_0$ on the undeformed axis of the beam is mapped to the point $G$ in $\mathscr{B}$, whose actual position $\boldsymbol{r} = \boldsymbol{r}(s)$ easily reads $\boldsymbol{r} = \boldsymbol{r}_0 + \boldsymbol{u}$, where $\boldsymbol{u} = \boldsymbol{u}(s) = u(s)\,\boldsymbol{T}_1 + v(s)\,\boldsymbol{T}_2 + w(s)\,\boldsymbol{T}_3$ is the displacement of $G_0$, and $u$, $v$, $w$ are the components of $\boldsymbol{u}$ along the beam axis and the principal directions of the cross section $\mathcal{A}_0$, respectively. On the other hand, the current cross-sectional orientations can be described by a field of orthonormal right-handed triads $\{\boldsymbol{t}_1(s), \boldsymbol{t}_2(s), \boldsymbol{t}_3(s)\}$ such that:

$$\boldsymbol{t}_i = \boldsymbol{\Lambda}\,\boldsymbol{T}_i = \boldsymbol{\Lambda}\,\boldsymbol{\Lambda}_0\,\boldsymbol{e}_i, \quad (i = 1, 2, 3) \quad \Rightarrow \quad \boldsymbol{\Lambda} = \sum_{i=1}^{3} \boldsymbol{t}_i \otimes \boldsymbol{T}_i, \tag{3}$$

where $\boldsymbol{\Lambda} = \boldsymbol{\Lambda}(s)$ is a two-point tensor that maps the local basis $\{\boldsymbol{T}_1, \boldsymbol{T}_2, \boldsymbol{T}_3\}$ onto the rotated actual one $\{\boldsymbol{t}_1, \boldsymbol{t}_2, \boldsymbol{t}_3\}$, and for this reason is known as the rotation tensor. Similarly to $\boldsymbol{\Lambda}_0$, also $\boldsymbol{\Lambda}$ must be a proper orthogonal tensor, that is $\boldsymbol{\Lambda} \in \mathrm{SO}(3)$. Note that, as a result of shear deformations, the cross sections in the actual configuration are not locally orthogonal to the line of centroids, and therefore the unit vector $\boldsymbol{t}_1$ is not tangent to the beam axis in the deformed configuration. With the previous definitions at hand, the admissible configuration space for the geometrically exact 3D beam can thus be defined as:

$$\mathscr{C} = \{s \mapsto (\boldsymbol{r}, \boldsymbol{\Lambda}) \,:\, [0, \ell] \mapsto \mathbb{R}^3 \times \mathrm{SO}(3)\}. \tag{4}$$

The main difficulty in representing the beam admissible configuration space $\mathscr{C}$ lies in the fact that $\boldsymbol{\Lambda} \in \mathrm{SO}(3)$, and SO(3) is not a linear space but a nonlinear differential manifold. This issue can be addressed by noting that the rotation tensor satisfies the properties defined in Eq. (2), which enables us to use a three-parameter description for $\boldsymbol{\Lambda}$ based on the (local) Euler rotation vector $\boldsymbol{\theta} = \boldsymbol{\theta}(s) = \phi(s)\,\boldsymbol{T}_1 + \chi(s)\,\boldsymbol{T}_2 + \psi(s)\,\boldsymbol{T}_3$, where $\phi$, $\chi$, $\psi$ denote the signed rotation angles about $\boldsymbol{T}_1$, $\boldsymbol{T}_2$ and $\boldsymbol{T}_3$, respectively. It is recalled that each skew-symmetric tensor $\mathbf{S}$ can be associated with a unique vector in $\mathbb{R}^3$, termed the axial vector of $\mathbf{S}$ and here denoted by $\mathrm{ax}(\mathbf{S})$, satisfying [21]:

$$\mathbf{S}\,\boldsymbol{a} = \mathrm{ax}(\mathbf{S}) \times \boldsymbol{a} \qquad \forall \boldsymbol{a} \in \mathbb{R}^3. \tag{5}$$

Thus, the rotation vector $\boldsymbol{\theta}$ is associated with a skew-symmetric tensor $\boldsymbol{\Theta}$, called the spin tensor, such that $\boldsymbol{\theta} = \mathrm{ax}(\boldsymbol{\Theta}) \iff \boldsymbol{\Theta} = \mathrm{spin}(\boldsymbol{\theta})$, where the operator spin is defined as:

$$\mathrm{spin}(\boldsymbol{\theta})\,\boldsymbol{a} = \boldsymbol{\theta} \times \boldsymbol{a} \qquad \forall \boldsymbol{a} \in \mathbb{R}^3. \tag{6}$$

The introduction of the spin tensor allows us to parameterize $\mathbf{\Lambda}$ by exploiting the Rodrigues formula [11,21]:

$$\mathbf{\Lambda} = \mathbf{I} + \frac{\sin(\theta)}{\theta}\mathbf{\Theta} + \frac{1-\cos(\theta)}{\theta^2}\mathbf{\Theta}^2 = \exp(\mathbf{\Theta}), \tag{7}$$

where $\theta = \|\boldsymbol{\theta}\|$ is the total rotation angle. Eq. (7) shows that the orthogonal rotation tensor $\mathbf{\Lambda}$ (which represents finite rotations), can be represented as a function of the Euler rotation vector only (via $\theta$ and $\mathbf{\Theta}$), and results from the exponential map applied to the skew-symmetric spin tensor $\mathbf{\Theta}$, which describes infinitesimal rotations. Notably, this implies that $\mathbf{\Theta}$ belongs to the tangent space of SO(3). Therefore, by assuming $\boldsymbol{\theta}$ as a primary variable, the beam configuration space becomes linear:

$$\mathscr{C} \to \mathscr{C}_\theta = \{s \mapsto (\boldsymbol{r}, \boldsymbol{\theta}) : [0, \ell] \mapsto \mathbb{R}^3 \times \mathbb{R}^3\}. \tag{8}$$

### 2.2. Generalized stress and strain measures

Consider a generic point $P_0 \in \mathcal{A}_0$ in $\mathscr{B}_0$, identified by the position vector $\boldsymbol{x}_{P_0}(s,\zeta_2,\zeta_3) = \boldsymbol{r}_0(s) + \boldsymbol{\zeta}_0(s,\zeta_2,\zeta_3)$ relative to the fixed basis, where $\boldsymbol{\zeta}_0(s,\zeta_2,\zeta_3) = \zeta_2\,\boldsymbol{T}_2(s) + \zeta_3\,\boldsymbol{T}_3(s)$ represents its position with respect to the centroid $G_0$ of the cross section $\mathcal{A}_0$ (see Fig. 1). Due to the kinematic assumptions on the cross sections previously introduced, the point $P_0$ is mapped in $\mathscr{B}$ to the point $P$ whose position vector $\boldsymbol{x}_P(s,\zeta_2,\zeta_3)$ is such that $\boldsymbol{x}_P = \boldsymbol{r}(s) + \boldsymbol{\zeta}(s,\zeta_2,\zeta_3)$, where $\boldsymbol{\zeta}(s,\zeta_2,\zeta_3) = \zeta_2\,\boldsymbol{t}_2(s) + \zeta_3\,\boldsymbol{t}_3(s)$ is the position vector of $P$ with respect to $G$. Thus, the generic initial cross section $\mathcal{A}_0$ is associated with the cross section $\mathcal{A}$ in the current configuration defined as the set $\mathcal{A} = \left\{P \in \mathbb{R}^3 \mid \boldsymbol{x}_P(s,\zeta_2,\zeta_3) = \boldsymbol{r}(s) + \boldsymbol{\zeta}(s,\zeta_2,\zeta_3)\right\}$.

As customary in beam theories, the generalized spatial stresses $\boldsymbol{n}$ and $\boldsymbol{m}$ acting on $\mathcal{A}$ can be introduced as the stress resultant and couple resultant, respectively, and are given by [14]:

$$\boldsymbol{n}(s) = \int_{\mathcal{A}} \boldsymbol{\sigma}\,\boldsymbol{t}_1\,\mathrm{d}a = \int_{\mathcal{A}_0} \mathbf{P}(s,\boldsymbol{\zeta}_0)\,\boldsymbol{T}_1\,\mathrm{d}A \tag{9}$$

$$\boldsymbol{m}(s) = \int_{\mathcal{A}} \boldsymbol{\zeta} \times \left(\boldsymbol{\sigma}\,\boldsymbol{t}_1\right)\mathrm{d}a = \int_{\mathcal{A}_0} \boldsymbol{\zeta} \times \left[\mathbf{P}(s,\boldsymbol{\zeta}_0)\,\boldsymbol{T}_1\right]\mathrm{d}A, \tag{10}$$

where $\boldsymbol{\sigma}$ is the Cauchy stress tensor, $\mathbf{P}$ is the first Piola-Kirchhoff stress tensor, $\mathrm{d}a$ and $\mathrm{d}A$ are the infinitesimal measures of area at the cross sections $\mathcal{A}$ and $\mathcal{A}_0$, respectively, and the Nanson's formula [43] has been applied in Eqs. (9) and (10). It is worth noting that the components of such spatial generalized stress measures are given relative to a spatial basis, but they can be more conveniently expressed with respect to the material basis performing a pull-back operation on the vector fields $\boldsymbol{n}$ and $\boldsymbol{m}$. Thus, the material stress resultant $\boldsymbol{N}$ and the material couple resultant $\boldsymbol{M}$ can be obtained as $\boldsymbol{N} = \mathbf{\Lambda}^{\mathrm{T}}\,\boldsymbol{n}$ and $\boldsymbol{M} = \mathbf{\Lambda}^{\mathrm{T}}\,\boldsymbol{m}$.

The material strain measures for the beam $\mathbf{\Gamma} = \mathbf{\Gamma}(s)$ and $\boldsymbol{K} = \boldsymbol{K}(s)$, work-conjugate to $\boldsymbol{N}$ and $\boldsymbol{M}$, respectively, were obtained by Simo [14] through the principle of virtual power:

$$\mathbf{\Gamma} = \mathbf{\Lambda}^{\mathrm{T}}\frac{\partial \boldsymbol{r}}{\partial s} - \boldsymbol{T}_1, \tag{11}$$

$$\boldsymbol{K} = \mathrm{ax}\left(\mathbf{\Lambda}^{\mathrm{T}}\frac{\partial \mathbf{\Lambda}}{\partial s}\right), \tag{12}$$

where $\mathbf{\Gamma}$ contains the axial and shear strains, while $\boldsymbol{K}$ the bending and torsional curvatures.

### 2.3. Balance equations, constitutive law and total potential energy

Denoting by $\overline{\boldsymbol{q}}(s)$ and $\overline{\boldsymbol{m}}(s)$ the external force and moments applied in $\mathscr{B}$ and expressed per unit of reference arc length, respectively, the material description of the equilibrium equations reads, for $s \in [0,\ell]$, as follows [14]:

$$\frac{\partial(\mathbf{\Lambda}\boldsymbol{N})}{\partial s} + \overline{\boldsymbol{q}}(s) = \mathbf{0}, \tag{13}$$

$$\frac{\partial(\mathbf{\Lambda}\boldsymbol{M})}{\partial s} + \overline{\boldsymbol{m}}(s) + \frac{\partial \boldsymbol{r}_0}{\partial s} \times (\mathbf{\Lambda}\boldsymbol{N}) = \mathbf{0}. \tag{14}$$

Collecting all the generalized material stress and strain measures in the vectors $\boldsymbol{F}^{\mathrm{T}} = \left[\boldsymbol{N}^{\mathrm{T}}, \boldsymbol{M}^{\mathrm{T}}\right]$ and $\boldsymbol{\varepsilon}^{\mathrm{T}} = \left[\mathbf{\Gamma}^{\mathrm{T}}, \boldsymbol{K}^{\mathrm{T}}\right]$, respectively, and referring to a linear hyperelastic material, the beam generalized constitutive law can be expressed as:

$$\boldsymbol{F}(s) = \tilde{\mathbf{C}}(s)\,\boldsymbol{\varepsilon}(s), \tag{15}$$

where $\tilde{\mathbf{C}}$ is the cross-sectional stiffness matrix. For initially curved beams, the generalized constitutive matrix in Eq. (15) can be obtained following the approach in [44] as $\tilde{\mathbf{C}} = \tilde{\mathbf{\Lambda}}\mathbf{C}\tilde{\mathbf{\Lambda}}^{\mathrm{T}}$, where $\mathbf{C}$ is the cross-sectional stiffness matrix if the local reference basis $\{\boldsymbol{T}_i\}_{i=1,2,3}$ coincides with the fixed basis $\{\boldsymbol{e}_i\}_{i=1,2,3}$, while $\tilde{\mathbf{\Lambda}} = \tilde{\mathbf{\Lambda}}(s)$ has the following block form:

$$\tilde{\mathbf{\Lambda}} = \begin{bmatrix} \mathbf{\Lambda}_0^{\mathrm{T}}(s) & \mathbf{0}_{3\times3} \\ \mathbf{0}_{3\times3} & \mathbf{\Lambda}_0^{\mathrm{T}}(s) \end{bmatrix}, \tag{16}$$

with $\mathbf{0}_{h\times k}$ denoting the $h$-by-$k$ matrix filled with zeros. Hence, the total potential energy of the beam $U = U(\boldsymbol{u},\boldsymbol{\theta})$ is given by:

$$U(\boldsymbol{u},\boldsymbol{\theta}) = \frac{1}{2}\int_0^\ell \boldsymbol{\varepsilon}^{\mathrm{T}}\tilde{\mathbf{C}}\boldsymbol{\varepsilon}\,\mathrm{d}s - \int_0^\ell \overline{\boldsymbol{q}}^{\mathrm{T}}\boldsymbol{u}\,\mathrm{d}s - \int_0^\ell \overline{\boldsymbol{m}}^{\mathrm{T}}\boldsymbol{\theta}\,\mathrm{d}s, \tag{17}$$

with $\boldsymbol{\varepsilon} = \boldsymbol{\varepsilon}(\boldsymbol{u}, \boldsymbol{\theta})$. It can be easily recognized that the first integral on the right-hand side of Eq. (17) represents the beam strain energy, while the last two terms correspond to the work of the external distributed loads $\overline{\boldsymbol{q}}$ and $\overline{\boldsymbol{m}}$. The solution $\{\boldsymbol{u}^*, \boldsymbol{\theta}^*\}$ to the beam boundary value problem described by Eqs. (11) to (15) can be obtained by minimizing the total potential energy: $\{\boldsymbol{u}^*, \boldsymbol{\theta}^*\} = \operatorname{argmin}_{\boldsymbol{u},\boldsymbol{\theta}} U$.

Without loss of generality, and for the sake of simplicity, in the subsequent applications, each $\mathcal{A}_0 \in \mathscr{A}_0$ is assumed to be symmetric with respect to at least one axis. As a result, the present formulation does not involve mutual shear correction factors. Furthermore, it is assumed that all cross sections in the family $\mathscr{A}_0$ are congruent, from which it follows that the cross-sectional area $A$, the principal moments of inertia $I_2$ and $I_3$, shear correction factors $\chi_2$ and $\chi_3$, and torsional constant $J_t$, are constant $\forall s \in [0, \ell]$. Lastly, the beam is assumed to be homogeneous and composed of an isotropic linear elastic material. Under these assumptions, the beam generalized stiffness matrix $\mathbf{C}$ is not dependent on the axial coordinate $s$ and takes the following diagonal form: $\mathbf{C} = \operatorname{diag}(EA, GA/\chi_2, GA/\chi_3, GJ_t, EI_2, EI_3)$, where $E$ and $G$ denote the Young's and shear moduli of the material, respectively.

## 3. Virtual element formulation for 3D beams

To numerically solve a nonlinear problem involving 3D beams in large-displacement and large-rotation regimes, a suitable discretization scheme must be introduced. Among many possibilities, we derive a VE formulation starting from the total potential energy defined in Eq. (17). The beam axis in its reference configuration is then partitioned into a collection $\Omega_h$ of $N$ non-overlapping straight 1D elements. The generic element $\Omega_e \in \Omega_h$ has length $l_e$, thus $\ell \simeq \sum_{e=1}^{N} l_e$. The mathematical foundations of the VE method are extensively developed in the literature, particularly in the papers by Beirão da Veiga and coauthors [39] and by Wriggers [27,40] for applications to the case of trusses and two-dimensional beams. The main aspects required to construct a VE formulation can be briefly summarized as follows.

Let $n \geq 1$ be a fixed integer index, and let $\varphi_1(\xi), \dots, \varphi_{n+1}(\xi) \in H^1(\Omega_e)$ be $n+1$ not explicitly known but linearly independent functions of the local coordinate $\xi \in [0, l_e]$ running along $\Omega_e$. Then, a local virtual element space $\mathcal{V}_h(\Omega_e)$ can be defined $\forall \Omega_e \in \Omega_h$ as:

$$\mathcal{V}_h(\Omega_e) = \left\{ p_h \in H^1(\Omega_e) \,:\, p_h = \sum_{i=1}^{n+1} \alpha_i \, \varphi_i(\xi), \;\; p_h(0) = a, \;\; p_h(l_e) = b \right\}, \tag{18}$$

where $a, b \in \mathbb{R}$ are known values, while $\alpha_i \in \mathbb{R}, \;\; \forall i = 1, \dots, n+1$. Basically, the local space $\mathcal{V}_h(\Omega_e)$ in this 1D framework is the set that contains all functions $p_h = p_h(\xi)$ that assume a known value only at the element boundary $\partial\Omega_e \equiv \{0, l_e\}$, but, unlike the FE method, do not have a known representation inside $\Omega_e$. Note that by construction $\dim(\mathcal{V}_h) = n+1$. A convenient set of $n+1$ degrees of freedom (DoF) for $\mathcal{V}_h$ will be introduced in Section 3.1.

Another key ingredient of the VE method is the definition of a projection operator $\Pi_n$ that maps the ansatz space $\mathcal{V}_h(\Omega_e)$ onto the space $\mathcal{P}_n(\Omega_e)$ of the $n$-degree polynomials defined on $\Omega_e$. The projector $\Pi_n$ enables the decomposition of any $p_h \in \mathcal{V}_h(\Omega_e)$ as $p_h = p_\pi^{(n)} + (p_h - p_\pi^{(n)})$, where the projected polynomial part $p_\pi^{(n)} = \Pi_n[p_h] \in \mathcal{P}_n(\Omega_e)$ is often referred to as the consistent part of $p_h$, while the complementary part $p_h - p_\pi^{(n)}$ ensures the stability of the virtual element. It is important to remark that, as proved by Wriggers [27], the VE procedure for one-dimensional geometries yields full-rank stiffness matrices even if only the consistent part is considered. Thus, there is no need to stabilize one-dimensional virtual elements.

The operator $\Pi_n$ is defined element-wise through the following conditions [27,39]:

$$\int_0^{l_e} \boldsymbol{\eta}_n' \left(p_\pi^{(n)}\right)' \mathrm{d}\xi = \int_0^{l_e} \boldsymbol{\eta}_n' \, p_h' \, \mathrm{d}\xi \tag{19}$$

$$\int_0^{l_e} p_\pi^{(n)} \, \mathrm{d}\xi = \int_0^{l_e} p_h \, \mathrm{d}\xi, \tag{20}$$

where $\boldsymbol{\eta}_n$ is a vector-valued $n$th degree polynomial weight function and the prime symbol denotes the derivative with respect to $\xi$. It can be observed from Eq. (19) that the projection operator $\Pi_n$ is defined to provide the best approximation within the element (in the square integral norm) of the gradient of the primary variable in the space of polynomials of degree $n$. Eq. (20) is instead introduced to fix the constant part of the projection $p_\pi^{(n)}$ [39].

The integral $\mathcal{I}^{(n)}$ on the right-hand side of Eq. (19) can be evaluated integrating by parts:

$$\mathcal{I}^{(n)} = \int_0^{l_e} \boldsymbol{\eta}_n' \, p_h' \, \mathrm{d}\xi = \left[\boldsymbol{\eta}_n' \, p_h\right]_0^{l_e} - \int_0^{l_e} \boldsymbol{\eta}_n'' \, p_h \, \mathrm{d}\xi. \tag{21}$$

Thus, since $p_h$ is known only at the element endpoints by construction, $\mathcal{I}^{(n)}$ is explicitly computable only in the case of linear ansatz, i.e. for $n = 1$ (since $\boldsymbol{\eta}_n'' = \mathbf{0}$). For $n \geq 2$ the term involving $\boldsymbol{\eta}_n''$ in Eq. (21) can be handled by defining the quantities

$$m_{(p),k} = \frac{1}{l_e^{k+1}} \int_0^{l_e} \xi^k \, p_h \, \mathrm{d}\xi, \qquad k = 0, 1, \dots, n-2 \tag{22}$$

as new element variables. These variables, which are not associated with any node, are referred to as moments or internal variables. Note that each moment $m_{(p),k}$ is scaled by the $(k+1)$th power of the element length to retain the same physical units as the associated primary variable $p$.

### 3.1. Computation of the projection for a generic ansatz

Following [27] and as detailed below, for a one-dimensional element, the consistent part $p_\pi^{(n)}(\xi)$ of the primary variable $p$ can be computed explicitly for a generic polynomial ansatz of degree $n$.

Let us define the vector $\mathsf{p}_e^{(n)} = \left[p_1, p_2, m_{(p),0}, m_{(p),1}, \dots, m_{(p),n-2}\right]^{\mathrm{T}}$, which collects the $n+1$ element unknowns for the $n$th degree ansatz, i.e.: the nodal values $p_1 = a$, $p_2 = b$ of the primary variable at the points $\xi = 0$ and $\xi = l_e$, respectively, as well as, if $n \geq 2$, the moments $m_{(p),0}, \dots, m_{(p),n-2}$ defined by Eq. (22). Since $p_\pi^{(n)} \in \mathcal{P}_n(\Omega_e)$, the following expression can be assumed for the projection:

$$p_\pi^{(n)}(\xi) = \sum_{j=0}^{n} c_j\, \xi^j = c_0 + \mathsf{N}_\pi^{(n)\mathrm{T}}\, \hat{\mathsf{c}}, \tag{23}$$

where $\mathsf{N}_\pi^{(n)} = \left[\xi, \xi^2, \dots, \xi^n\right]^{\mathrm{T}}$ is a vector that contains all univariate monomials of $\xi$ up to the order $n$, while $c_0$ and the elements of $\hat{\mathsf{c}} = \left[c_1, c_2, \dots, c_n\right]^{\mathrm{T}}$ are coefficients to be determined.

The coefficient $c_0$ can be easily obtained, $\forall n$, as $c_0 = p_1$ by observing that the ansatz function $p_h$ must retain the value at the first node for $\xi = 0$. This result is rigorously proved in Appendix A. With regard to the remaining coefficients, they can be explicitly computed following the procedure described below.

The first derivative of the projection, $p_\pi^{(n)\prime} = \frac{\mathrm{d}p_\pi^{(n)}}{\mathrm{d}\xi}$, is given by:

$$p_\pi^{(n)\prime} = \sum_{j=1}^{n} j\, c_j\, \xi^{j-1} = \mathsf{B}_\pi^{(n)\mathrm{T}}\, \hat{\mathsf{c}}, \tag{24}$$

where $\mathsf{B}_\pi^{(n)} = \left[1, 2\xi, \dots, n\xi^{n-1}\right]^{\mathrm{T}} = \mathsf{N}_\pi^{(n)\prime}$. Now, assuming $\boldsymbol{\eta}_n' = \mathsf{B}_\pi^{(n)}$, the integral $\mathcal{I}^{(n)}$ on the right-hand side of Eq. (19) can be computed in two different ways. On the one hand, the ansatz for the projection in Eqs. (23) and (24) yields:

$$\mathcal{I}^{(n)} = \int_0^{l_e} \boldsymbol{\eta}_n'\, p_\pi^{(n)\prime}\, \mathrm{d}\xi = \int_0^{l_e} \mathsf{B}_\pi^{(n)} \mathsf{B}_\pi^{(n)\mathrm{T}}\, \hat{\mathsf{c}}\, \mathrm{d}\xi = \mathsf{G}\, \hat{\mathsf{c}}, \tag{25}$$

where the $n \times n$ matrix $\mathsf{G}$ (symmetric by construction) is given in closed form as:

$$\mathsf{G} = \int_0^{l_e} \begin{bmatrix} 1 \\ 2\xi \\ \vdots \\ n\xi^{n-1} \end{bmatrix} \begin{bmatrix} 1 & 2\xi & \dots & n\xi^{n-1} \end{bmatrix} \mathrm{d}\xi = \begin{bmatrix} l_e & l_e^2 & \dots & l_e^n \\ l_e^2 & \frac{4}{3} l_e^3 & \dots & \frac{2n}{n+1} l_e^{n+1} \\ \vdots & \vdots & \ddots & \vdots \\ l_e^n & \frac{2n}{n+1} l_e^{n+1} & \dots & \frac{n^2}{2n-1} l_e^{2n-1} \end{bmatrix}. \tag{26}$$

On the other hand, recalling the definition of the moments in Eqs. (22), (21) leads to:

$$\begin{aligned} \mathcal{I}^{(n)} &= \left[\mathsf{B}_\pi^{(n)} p_h\right]_0^{l_e} - \int_0^{l_e} \mathsf{B}_\pi^{(n)\prime} p_h\, \mathrm{d}\xi = \\ &= \mathsf{B}_\pi^{(n)}(l_e)\, p_h(l_e) - \mathsf{B}_\pi^{(n)}(0)\, p_h(0) - \int_0^{l_e} \begin{bmatrix} 0 \\ 2p_h \\ \vdots \\ n(n-1)\xi^{n-2} p_h \end{bmatrix} \mathrm{d}\xi = \\ &= \begin{bmatrix} 1 \\ 2l_e \\ \vdots \\ n l_e^{n-1} \end{bmatrix} p_2 - \begin{bmatrix} 1 \\ 0 \\ \vdots \\ 0 \end{bmatrix} p_1 - \begin{bmatrix} 0 \\ 2l_e m_0 \\ \vdots \\ n(n-1) l_e^{n-1} m_{n-2} \end{bmatrix} = \\ &= \begin{bmatrix} p_2 - p_1 \\ 2l_e p_2 - 2l_e m_0 \\ \vdots \\ n l_e^{n-1} p_2 - n(n-1) l_e^{n-1} m_{n-2} \end{bmatrix} = \mathsf{A}\, \mathsf{p}_e^{(n)}, \end{aligned} \tag{27}$$

with $\mathsf{A}$ being the $n \times (n+1)$ matrix that collects the coefficients of $\mathcal{I}^{(n)}$ relative to the element variables $\mathsf{p}_e^{(n)}$:

$$\mathsf{A} = \begin{bmatrix} -1 & 1 & 0 & \dots & 0 \\ 0 & 2l_e & -2l_e & \dots & 0 \\ \vdots & \vdots & \vdots & \ddots & \vdots \\ 0 & n l_e^{n-1} & 0 & \dots & n(n-1) l_e^{n-1} \end{bmatrix}. \tag{28}$$

Hence, comparing Eqs. (25) and (27) and defining the matrix $\mathsf{H} = \mathsf{G}^{-1}\, \mathsf{A}$, the vector of coefficients $\hat{\mathsf{c}}$ can be readily obtained as a function of the element nodal and internal variables:

$$\hat{\mathsf{c}} = \mathsf{H}\, \mathsf{p}_e^{(n)}. \tag{29}$$

Once the coefficients $\hat{\mathsf{c}}$ and $c_0$ are known, the projection $p_\pi^{(n)}$ is computable and can be recast in terms of the element nodal and internal variables by defining an $(n+1) \times (n+1)$ constant matrix $\mathsf{P}^{(n)}$, termed the projection matrix, such that:

$$p_\pi^{(n)}(\xi) = \mathsf{N}_{\pi,0}^{(n)}(\xi)^{\mathrm{T}} \mathsf{P}^{(n)}\, \mathsf{p}_e^{(n)}, \tag{30}$$

where $\mathsf{N}_{\pi,0}^{(n)\,\mathrm{T}} = \left[1, \mathsf{N}_{\pi}^{(n)\mathrm{T}}\right]$ and the projection matrix has the following block form:

$$\mathsf{P}^{(n)} = \begin{bmatrix} 1 & \mathbf{0}_{1\times n} \\ & \mathsf{H} \end{bmatrix}. \tag{31}$$

In [27] and [40] the projection for a generic variable $p_{\pi}^{(n)}$ was explicitly computed for linear, quadratic and cubic ansatz spaces using the approach defined previously. For completeness, all the relevant quantities necessary to compute the projection are briefly reported below.

(a) **Linear ansatz** ($n = 1$)

- Vector of the element unknowns: $\mathsf{p}_e^{(1)} = \left[p_1, p_2\right]^{\mathrm{T}}$.
- Ansatz for the projection: $p_{\pi}^{(1)} = c_0 + c_1\xi \quad \Rightarrow \quad \mathsf{N}_{\pi,0}^{(1)} = [1, \xi]^{\mathrm{T}}$.
- Matrix G and its inverse: $\mathsf{G} = [l_e] \quad \Rightarrow \quad \mathsf{G}^{-1} = \left[\frac{1}{l_e}\right]$.
- Matrices A and H: $\mathsf{A} = \begin{bmatrix}-1 & 1\end{bmatrix}, \quad \mathsf{H} = \frac{1}{l_e}\begin{bmatrix}-1 & 1\end{bmatrix}$.
- Projection matrix: $\mathsf{P}^{(1)} = \frac{1}{l_e}\begin{bmatrix} l_e & 0 \\ -1 & 1 \end{bmatrix}$.

(b) **Quadratic ansatz** ($n = 2$)

- Vector of the element unknowns: $\mathsf{p}_e^{(2)} = \left[p_1, p_2, m_{(p),0}\right]^{\mathrm{T}}$.
- Ansatz for the projection: $p_{\pi}^{(2)} = c_0 + c_1\xi + c_2\xi^2 \quad \Rightarrow \quad \mathsf{N}_{\pi,0}^{(2)} = \left[1, \xi, \xi^2\right]^{\mathrm{T}}$.
- Matrix G and its inverse: $\mathsf{G} = \begin{bmatrix} l_e & l_e^2 \\ l_e^2 & \frac{4}{3}l_e^3 \end{bmatrix} \quad \Rightarrow \quad \mathsf{G}^{-1} = \frac{1}{l_e^3}\begin{bmatrix} 4l_e^2 & -3l_e \\ -3l_e & 3 \end{bmatrix}$.
- Matrices A and H: $\mathsf{A} = \begin{bmatrix}-1 & 1 & 0 \\ 0 & 2l_e & -2l_e\end{bmatrix}, \quad \mathsf{H} = \frac{1}{l_e^2}\begin{bmatrix}-4l_e & -2l_e & 6l_e \\ 3 & 3 & -6\end{bmatrix}$.
- Projection matrix: $\mathsf{P}^{(2)} = \frac{1}{l_e^2}\begin{bmatrix} l_e^2 & 0 & 0 \\ -4l_e & -2l_e & 6l_e \\ 3 & 3 & -6 \end{bmatrix}$.

(c) **Cubic ansatz** ($n = 3$)

- Vector of the element unknowns: $\mathsf{p}_e^{(3)} = \left[p_1, p_2, m_{(p),0}, m_{(p),1}\right]^{\mathrm{T}}$.
- Ansatz for the projection: $p_{\pi}^{(3)} = c_0 + c_1\xi + c_2\xi^2 + c_3\xi^3 \quad \Rightarrow \quad \mathsf{N}_{\pi,0}^{(3)} = \left[1, \xi, \xi^2, \xi^3\right]^{\mathrm{T}}$.
- Matrix G and its inverse:

$$\mathsf{G} = \begin{bmatrix} l_e & l_e^2 & l_e^3 \\ l_e^2 & \frac{4}{3}l_e^3 & \frac{3}{2}l_e^4 \\ l_e^3 & \frac{3}{2}l_e^4 & \frac{9}{5}l_e^5 \end{bmatrix} \quad \Rightarrow \quad \mathsf{G}^{-1} = \frac{1}{l_e^5}\begin{bmatrix} 9l_e^4 & -18l_e^3 & 10l_e^2 \\ -18l_e^3 & 48l_e^2 & -30l_e \\ 10l_e^2 & -30l_e & 20 \end{bmatrix}.$$

- Matrices A and H:

$$\mathsf{A} = \begin{bmatrix}-1 & 1 & 0 & 0 \\ 0 & 2l_e & -2l_e & 0 \\ 0 & 3l_e^2 & 0 & -6l_e^2\end{bmatrix}, \quad \mathsf{H} = \frac{1}{l_e^3}\begin{bmatrix}-9l_e^2 & 3l_e^2 & 36l_e^2 & -60l_e^2 \\ 18l_e & -12l_e & -96l_e & 180l_e \\ -10 & 10 & 60 & -120\end{bmatrix}.$$

- Projection matrix: $\mathsf{P}^{(3)} = \frac{1}{l_e^3}\begin{bmatrix} l_e^3 & 0 & 0 & 0 \\ -9l_e^2 & 3l_e^2 & 36l_e^2 & -60l_e^2 \\ 18l_e & -12l_e & -96l_e & 180l_e \\ -10 & 10 & 60 & -120 \end{bmatrix}$.

### 3.2. Numerical implementation of three-dimensional beam virtual elements

The total potential energy in Eq. (17) can be considered as the starting point for an efficient numerical implementation of geometrically exact 3D beam virtual elements. As discussed, for example, by Wriggers [27], a locking-free formulation can be obtained for two-dimensional beams by adopting a polynomial interpolation for the deflections which is one order higher than that of the rotation. This approach is effective because it ensures consistency in the approximation of the generalized strains, which depend on both the rotations and the first derivatives of the displacements. By examining the mathematical form of the strain measures defined in Eqs. (11) and (12), it can be assumed that a similar rationale holds also for three-dimensional beams. Hence, the virtual elements defined in the following have been built considering a discretization of displacements and rotations with different interpolation orders, generally higher for the displacement components $u$, $v$, $w$ than for the rotations $\phi$, $\chi$, $\psi$.

Following this strategy, two distinct virtual elements for 3D beams have been constructed:

- a first element employing a linear ansatz for the rotations and a quadratic ansatz for the displacement components (referred to as the VEB-1 element in the following).
- a second element based on a quadratic ansatz for the rotations and a cubic ansatz for the displacement components (referred to as the VEB-2 element in the following).

In both cases, recalling Eq. (30), the consistent part $p_\pi$ of each displacement and rotation component $p$ (where the symbol $p$ can represent $u, v, w, \phi, \chi, \psi$) assumes the following form:

$$p_\pi = p_\pi^{(n)} = \mathsf{N}_{\pi,0}^{(n)\,\mathrm{T}}\,\mathsf{P}^{(n)}\,\mathsf{p}_e^{(n)} \qquad \text{if } p \in \{\phi, \chi, \psi\} \tag{32}$$

$$p_\pi = p_\pi^{(n+1)} = \mathsf{N}_{\pi,0}^{(n+1)\,\mathrm{T}}\,\mathsf{P}^{(n+1)}\,\mathsf{p}_e^{(n+1)} \qquad \text{if } p \in \{u, v, w\} \tag{33}$$

where the values $n = 1$ and $n = 2$ identify the virtual elements VEB-1 and VEB-2, respectively, and the vector $\mathsf{p}_e^{(n)}$, with $\mathsf{p} \in \{\mathsf{u}, \mathsf{v}, \mathsf{w}, \boldsymbol{\phi}, \boldsymbol{\chi}, \boldsymbol{\psi}\}$, here collects the element unknowns associated with the variable $p$ for the $n$th degree ansatz. Hence, for instance, $\mathsf{v}_e^{(3)} = \{v_1, v_2, m_{(v),0}, m_{(v),1}\}$, and $\boldsymbol{\phi}_e^{(2)} = \{\phi_1, \phi_2, m_{(\phi),0}\}$. As a result, the VEB-1 element has 15 DoF, of which 3 are moments, while the VEB-2 element has 21 DoF, of which 9 are moments.

It is important to note that, in general, torsion and bending are coupled. Therefore, a possible benefit in terms of accuracy could be achieved by adopting the same discretization ansatz for both the axial component of the rotation vector and the displacements. To explore this possibility, we have constructed two additional virtual elements:

- an element based on a linear ansatz for the rotations $\chi$, $\psi$, and on a quadratic ansatz for the displacement components as well as for the axial rotation $\phi$ (referred to as the VEB-1T element in the following).
- an element based on a quadratic ansatz for the rotations $\chi$, $\psi$, and on a cubic ansatz for the displacement components as well as for the axial rotation $\phi$ (referred to as the VEB-2T element in the following).

In both cases, recalling again Eq. (30), the projected part $p_\pi$ of each displacement and rotation component $p$ (with $p \in \{u, v, w, \phi, \chi, \psi\}$) reads:

$$p_\pi = p_\pi^{(n)} = \mathsf{N}_{\pi,0}^{(n)\,\mathrm{T}}\,\mathsf{P}^{(n)}\,\mathsf{p}_e^{(n)} \qquad \text{if } p \in \{\chi, \psi\} \tag{34}$$

$$p_\pi = p_\pi^{(n+1)} = \mathsf{N}_{\pi,0}^{(n+1)\,\mathrm{T}}\,\mathsf{P}^{(n+1)}\,\mathsf{p}_e^{(n+1)} \qquad \text{if } p \in \{u, v, w, \phi\} \tag{35}$$

where $n = 1$ and $n = 2$ identify the virtual elements VEB-1T and VEB-2T. As a consequence of this different ansatz, the VEB-1T element has 16 DoF, of which 4 are moments, while the VEB-2T element has 22 DoF, of which 10 moments.

All the virtual elements described above have been implemented through customized codes using the Mathematica package AceGen (Wolfram Mathematica, v. 14.1), a hybrid numeric-symbolic tool that allows automated computational modeling [45].

For each virtual element, an element-wise approximation $U_h$ of the total potential energy $U$ in Eq. (17) can be achieved as follows. With reference, for instance, to the VEB-$n$ elements (with $n = 1$ or $n = 2$), the approximated expressions $\boldsymbol{u}_h^{(n+1)}$ and $\boldsymbol{\theta}_h^{(n)}$ for the displacement field of the beam axis $\boldsymbol{u}$ and the rotation vector $\boldsymbol{\theta}$ are obtained from Eqs. (33) and (32), respectively, noting that the projection matrix $\mathsf{P}^{(n)}$ and the vector of monomials $\mathsf{N}_{\pi,0}^{(n)}$ are fixed quantities for a given $n$:

$$\boldsymbol{u}_h^{(n+1)} = \left(\mathsf{N}_{\pi,0}^{(n+1)\,\mathrm{T}}\mathsf{P}^{(n+1)}\mathsf{u}_e^{(n+1)}\right)\boldsymbol{T}_1 + \left(\mathsf{N}_{\pi,0}^{(n+1)\,\mathrm{T}}\mathsf{P}^{(n+1)}\mathsf{v}_e^{(n+1)}\right)\boldsymbol{T}_2 + \left(\mathsf{N}_{\pi,0}^{(n+1)\,\mathrm{T}}\mathsf{P}^{(n+1)}\mathsf{w}_e^{(n+1)}\right)\boldsymbol{T}_3, \tag{36}$$

$$\boldsymbol{\theta}_h^{(n)} = \left(\mathsf{N}_{\pi,0}^{(n)\,\mathrm{T}}\mathsf{P}^{(n)}\boldsymbol{\phi}_e^{(n)}\right)\boldsymbol{T}_1 + \left(\mathsf{N}_{\pi,0}^{(n)\,\mathrm{T}}\mathsf{P}^{(n)}\boldsymbol{\chi}_e^{(n)}\right)\boldsymbol{T}_2 + \left(\mathsf{N}_{\pi,0}^{(n)\,\mathrm{T}}\mathsf{P}^{(n)}\boldsymbol{\psi}_e^{(n)}\right)\boldsymbol{T}_3. \tag{37}$$

From these relationships, the approximated current position of the beam axis reads $\boldsymbol{r}_h = \boldsymbol{r}_0 + \boldsymbol{u}_h^{(n+1)}$. On the other hand, $\boldsymbol{\theta}_h^{(n)}$ enables the determination of approximate expressions for the spin tensor $\boldsymbol{\Theta}_h$ and the total rotation angle $\theta_h$ as $\boldsymbol{\Theta}_h = \mathrm{spin}(\boldsymbol{\theta}_h^{(n)})$ and $\theta_h = \left\|\boldsymbol{\theta}_h^{(n)}\right\|$, from which the approximation of the rotation tensor $\boldsymbol{\Lambda}_h$ can be computed via the exponential map: $\boldsymbol{\Lambda}_h = \exp(\boldsymbol{\Theta}_h)$. The strain measures in Eqs. (11)-(12) can then be approximated as:

$$\boldsymbol{\Gamma}_h = \boldsymbol{\Lambda}_h^{\mathrm{T}}\frac{\partial \boldsymbol{r}_h}{\partial \xi} - \boldsymbol{T}_1 \tag{38}$$

$$\boldsymbol{K}_h = \mathrm{ax}\left(\boldsymbol{\Lambda}_h^{\mathrm{T}}\frac{\partial \boldsymbol{\Lambda}_h}{\partial \xi}\right), \tag{39}$$

leading to the vector of generalized strain $\boldsymbol{\varepsilon}_h^{\mathrm{T}} = \left[\boldsymbol{\Gamma}_h^{\mathrm{T}}, \boldsymbol{K}_h^{\mathrm{T}}\right]$. Substituting the approximations for the strains (Eqs. (38) and (39)) in Eq. (17) yields an approximate expression of the element-wise total potential energy as dependent only on the unknowns related to the ansatz functions, namely the nodal displacements and rotations, as well as the moments. Combining these element variables into a unique vector $\hat{\mathsf{p}}_e^{(n)} = \left[u_1, u_2, v_1, v_2, \ldots, \psi_1, \psi_2, m_{(u),0}, \ldots, m_{(\psi),n-2}\right]^{\mathrm{T}}$, the element-wise approximated total potential energy is given by:

$$U_h\left(\hat{\mathsf{p}}_e^{(n)}\right) = \frac{1}{2}\int_0^{l_e} \boldsymbol{\varepsilon}_h^{\mathrm{T}}\left(\hat{\mathsf{p}}_e^{(n)}\right)\mathbf{C}\boldsymbol{\varepsilon}_h\left(\hat{\mathsf{p}}_e^{(n)}\right)\mathrm{d}\xi - \int_0^{l_e} \overline{\boldsymbol{q}}^{\mathrm{T}}\,\boldsymbol{u}_h^{(n+1)}\left(\hat{\mathsf{p}}_e^{(n)}\right)\mathrm{d}\xi - \int_0^{l_e} \overline{\boldsymbol{m}}^{\mathrm{T}}\,\boldsymbol{\theta}_h^{(n)}\left(\hat{\mathsf{p}}_e^{(n)}\right)\mathrm{d}\xi, \tag{40}$$

from which the element-wise residual $\mathsf{r}_e^{(n)}$ and tangent matrix $\mathsf{K}_e^{(n)}$ follow:

$$\mathsf{r}_e^{(n)} = \frac{\mathrm{d}U_h}{\mathrm{d}\hat{\mathsf{p}}_e^{(n)}} \quad \Rightarrow \quad \mathsf{K}_e^{(n)} = \frac{\mathrm{d}\mathsf{r}_e^{(n)}}{\mathrm{d}\hat{\mathsf{p}}_e^{(n)}}. \tag{41}$$

The global vector of the primary variables, the residual, and the tangent matrix are then obtained by a standard assembly procedure.

It is important to note that the element-wise tangent stiffness matrix $\mathsf{K}_e^{(n)}$ also contains the coefficients associated with the internal DoF, whose explicit determination is not strictly necessary. To reduce computational complexity while mitigating potential difficulties

that would arise in the physical interpretation of the boundary conditions related to the internal moments, a static condensation of the internal variables has been performed. The elimination of the moments has thus allowed the system of equations to be expressed solely in terms of the nodal DoF, facilitating the numerical solution procedure and ensuring a more streamlined and computationally efficient formulation. To this aim, the residual $\mathsf{r}_e^{(n)}$, the vector of the element unknowns $\hat{\mathsf{p}}_e^{(n)}$, and the tangent matrix $\mathsf{K}_e^{(n)}$ have been split in subvectors and submatrices related only to the nodal variables (subscript $u$) or the moments (subscript $m$):

$$\hat{\mathsf{p}}_e^{(n)} = \begin{bmatrix} \hat{\mathsf{p}}_{e,u}^{(n)} \\ \hat{\mathsf{p}}_{e,m}^{(n)} \end{bmatrix}, \qquad \mathsf{r}_e^{(n)} = \begin{bmatrix} \mathsf{r}_{e,u}^{(n)} \\ \mathsf{r}_{e,m}^{(n)} \end{bmatrix}, \qquad \mathsf{K}_e^{(n)} = \begin{bmatrix} \mathsf{K}_{e,uu}^{(n)} & \mathsf{K}_{e,um}^{(n)} \\ \mathsf{K}_{e,mu}^{(n)} & \mathsf{K}_{e,mm}^{(n)} \end{bmatrix}. \tag{42}$$

The internal variables are then removed via the Schur complement $\overline{\mathsf{K}}_{e,uu}^{(n)} = \mathsf{K}_{e,uu}^{(n)} - \mathsf{K}_{e,um}^{(n)}(\mathsf{K}_{e,mm}^{(n)})^{-1}\mathsf{K}_{e,mu}^{(n)}$, leading to the final reduced system of equations:

$$\overline{\mathsf{K}}_{e,uu}^{(n)}\,\hat{\mathsf{p}}_{e,u}^{(n)} = \overline{\mathsf{r}}_{e,u}^{(n)}, \tag{43}$$

with $\overline{\mathsf{r}}_{e,u}^{(n)} = \mathsf{r}_{e,u}^{(n)} - \mathsf{K}_{e,um}^{(n)}(\mathsf{K}_{e,mm}^{(n)})^{-1}\,\mathsf{r}_{e,m}$. A similar procedure has been followed to obtain the VEB-$n$T elements ($n = 1, 2$).

Due to the static condensation, each implemented VE retains only 12 DoF regardless of the degree chosen for the polynomial ansatz functions. It is important to emphasize that the condensation of the internal variables is performed element-wise. Thus, the (marginal) increase in computational cost related to condensation is paid only at the element level, but it does not affect significantly the overall cost of the simulation. It is also worth noting that the proposed formulation benefits from the use of a hybrid numeric-symbolic implementation, enabling the consistent and automatic differentiation of the element-wise total potential energy functional in Eq. (40), as discussed in [45]. Hence, in contrast to most existing techniques, our approach eliminates the need to manually approximate or implement the derivative of the exponential map.

Given the nonlinear nature of the problem, an incremental iterative procedure based on the Newton-Raphson method has been employed in numerical applications. Equilibrium configurations have been computed by resorting to either an arc-length control scheme when instability phenomena are expected, or a load-control scheme otherwise. For further details on the numerical implementation of such procedures, the reader is referred to [45].

## 4. Numerical examples

To demonstrate the effectiveness of the proposed formulation, this section presents a series of benchmark tests, well-established in the literature, that involve the analysis of various structures undergoing large deflections and rotations. These tests enable to assess the accuracy of the proposed VE framework for the description of 3D geometrically exact beams, as well as the convergence behavior of the virtual elements based either on the linear/quadratic or quadratic/cubic formulations. In all numerical applications shown in the following, the geometry has been constructed by defining a set of points in the three-dimensional Euclidean space connected by straight segments, giving rise to a polygonal chain representation of the reference geometry. All computations have been performed using the Mathematica package AceFEM [45]. The results obtained have been subsequently post-processed by developing tailored scripts in MATLAB (v. R2022a, MathWorks, MA, USA).

### 4.1. Crisfield's L-shaped cantilever

This first benchmark is taken from the work of Crisfield and Jelenić [46], later reconsidered also by Ibrahimbegovic and Taylor [42]. An L-shaped frame, initially placed in the horizontal plane $\{\boldsymbol{e}_1, \boldsymbol{e}_2\}$, is clamped at one end and loaded with an out-of-plane (i.e., along the direction $\boldsymbol{e}_3$) concentrated force $F$ at the other free end (see Fig. 2), assuming a final force value $F^* = 5\,\mathrm{N}$. The length of both legs of the frame is $L = 10\,\mathrm{m}$, and the material and section properties, reported in Fig. 2(a), are taken equal as those used in [42].

Since no analytical solution is available for this example, the problem is first solved numerically with the proposed VE framework, using a very fine discretization consisting of $10^4$ VEB-2T elements for each beam of the frame, and applying the final force value incrementally setting the maximum load increment to $\Delta F = F^*/10$. This analysis yields displacement components of the free end in very good agreement with other available numerical solutions. For example, the vertical displacement of the tip obtained with the proposed framework is $w_{\mathrm{r}} = 6.76848\,\mathrm{m}$, very close to the value 6.76847 m found by Jelenić and Crisfield [46]. Fig. 2(b) shows some illustrative deformed configurations assumed by the centroidal line of the frame for three values of the applied out-of-plane force $F$.

Subsequently, the value $w_{\mathrm{r}}$ has been used as a reference for a study aimed at assessing the convergence performance of the four 3D beam virtual elements developed. This convergence analysis is based on a series of seven meshes with an increasing level of refinement, where the $N$th mesh (with $N \in \{1, 2, \dots, 7\}$) consists of $2^{N-1}$ elements for each leg. Recalling that each VE has 12 DoF as a result of the static condensation procedure, the total number of DOF for the $N$th mesh is equal to $12 \cdot 2^N$. The results obtained are reported in Fig. 2(c), which shows plots of the relative error $\epsilon_w = |w_N - w_{\mathrm{r}}|/w_{\mathrm{r}}$ between the out-of-plane displacement component of the free end $w_N$ obtained with the level $N$ of discretization and the reference solution $w_{\mathrm{r}}$, as a function of the number of DoF. In particular, the rate of convergence of the VEB-2 and VEB-2T elements is twice the one of the VEB-1 and VEB-1T elements, with slightly better performance achieved if a higher-order interpolation is used for the axial component of the Euler rotation vector in the case of linear/quadratic ansatz. It can be seen that all the virtual beam elements implemented do not show locking. Moreover, it is interesting to note the remarkable level of accuracy of coarse meshes for the elements based on the quadratic/cubic ansatz, since even a mesh consisting of only one beam element per leg yields a relative error with respect to the reference solution $\epsilon_w \simeq 0.01\,\%$.

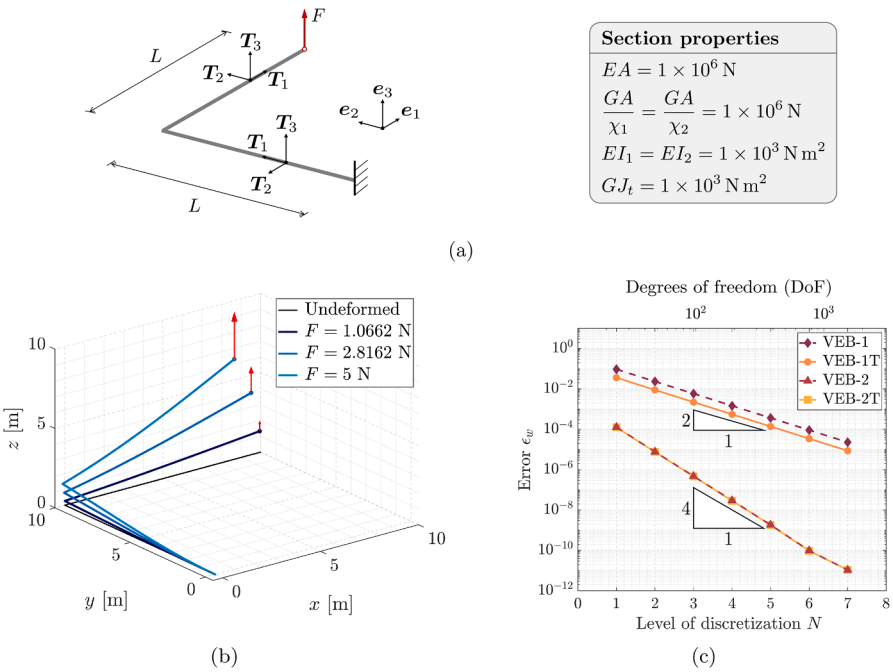


**Fig. 2.** Crisfield's L-shaped cantilever. (a) Problem description and notation. Problem data are taken from [42,46]. (b) Sequence of three illustrative deformed configurations of the cantilever in the case of a final applied force $F^* = 5\,\mathrm{N}$. (c) Convergence behavior of the various 3D beam virtual elements implemented. Plots of the relative error $\epsilon_w$ of the vertical displacement component $w$ of the tip under a force value $F^* = 5\,\mathrm{N}$ vs. the mesh refinement level.

### 4.2. *Lateral buckling of Lee's frame*

To investigate the response of the proposed VE formulation in the case of buckling, we consider the Lee's frame, a well-known benchmark, see e.g. [27]. A double-hinged L-shaped frame having equal height and length $L = 10\,\mathrm{m}$, depicted in Fig. 3(a), is loaded by a downward (i.e., along the $-\boldsymbol{e}_2$ direction) concentrated force $F$ having final value $F^* = 200\,\mathrm{N}$ and acting on the top beam at a distance $L/5$ from the right-angle corner of the frame. To investigate the performance of the proposed VE formulation in a three-dimensional framework, this example has been revisited. Here, the vertical point load has been applied with a small out-of-plane eccentricity $e$ with respect to the central axis of the top beam (in the $\boldsymbol{e}_3$ direction), thus inducing a twisting moment. The geometrical and material parameters assumed in this case are reported in Fig. 3(a). Both beams of the frame are assumed to be made of a linear elastic material with zero Poisson's ratio and Young's modulus $E = 100\,\mathrm{MPa}$, while the cross section is a square having an edge length $a = 10\,\mathrm{cm}$. The value of the eccentricity is set to $e = a/50$, which produces an applied concentrated torque $M_t = Fa/50$, whose final value is $M_t^* = 2/5\,\mathrm{N\,m}$.

In a first analysis, the unstable behavior of the structure has been investigated, discretizing each leg of the frame with $10^3$ VEB-2T virtual elements. The equilibrium path for the loaded point has been computed in terms of the vertical and out-of-plane displacement components $v$ and $w$ using the arc-length method. The full load-displacement plot is shown in Fig. 3(b), where the vertical force value $F$ and the displacement components have been normalized with respect to a load reference value $F_0 = 1\,\mathrm{N}$ and to the length $L$ of each beam of the frame, respectively. The lateral buckling of the frame occurs for a critical load value $F_{\mathrm{cr}} \simeq 84.4232\,\mathrm{N}$. This evidence is also confirmed by observing the four deformed configurations assumed by the frame prior to buckling shown in Fig. 3(c).

Subsequently, a force value of $84\,\mathrm{N}$, slightly lower than $F_{\mathrm{cr}}$, is selected to assess the convergence performance of the four virtual elements. In this case, reference is made to the out-of-plane displacement component at the loaded point, which is approximately equal to $w_{\mathrm{r}} = 2.03057328\,\mathrm{m}$ for this force value. As in the previous example, the analytical solution to this problem is not known. As such, the "converged" solution has been obtained using a very fine discretization consisting of $10^4$ VEB-2T virtual elements for each beam of the frame. The convergence analysis has been conducted on a series of 7 meshes, where the $N$th mesh ($N \in \{1, 2, \dots, 7\}$) consists of $10 \cdot 2^{N-1}$ elements per leg and therefore has $120 \cdot 2^N$ DoF. Fig. 3(d) reports the plots of the relative error $\epsilon_w = |w_N - w_{\mathrm{r}}|/w_{\mathrm{r}}$ between the reference solution $w_{\mathrm{r}}$ and the out-of-plane displacement component $w_N$ of the loaded point obtained with the $N$th discretization level, as a function of $N$. Similar considerations as in the previous example can be drawn with regard to the convergence rate of the various VEs implemented. However, in this case, a better performance in terms of absolute error (hence, with the convergence order remaining equal) has been attained if higher-order interpolation functions are adopted for the axial component of the rotation vector.

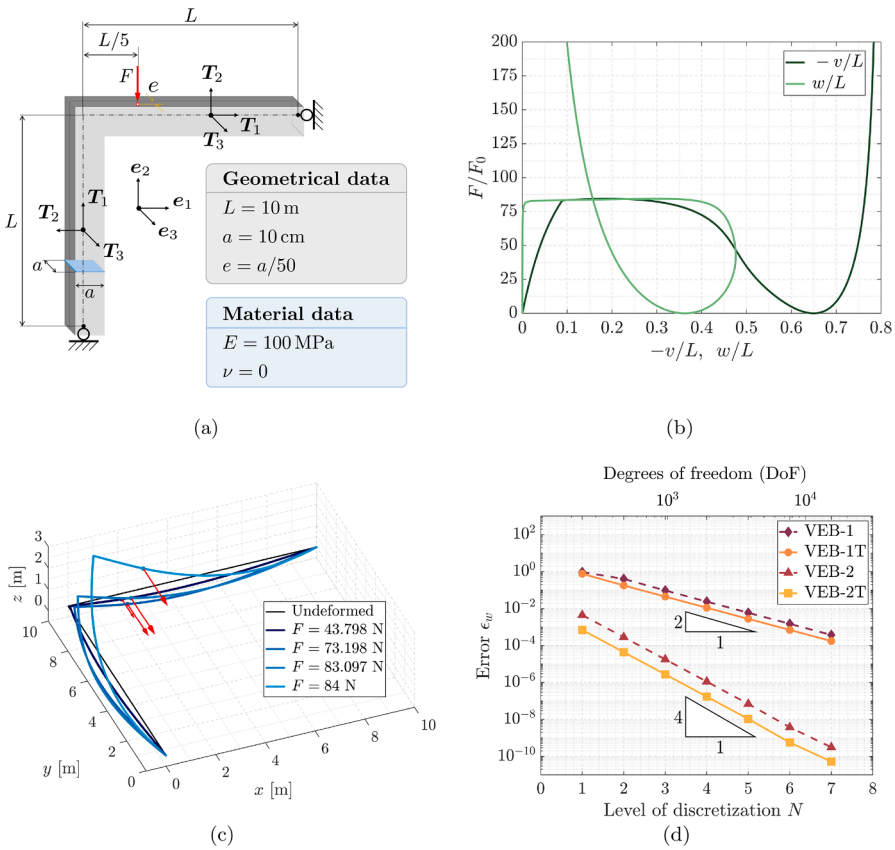


**Fig. 3.** Lee's frame with lateral buckling. (a) Problem description and notation. (b) Equilibrium paths of the dimensionless vertical and lateral displacement components $-v/L$ and $w/L$ of the loaded point for an applied final force value $F^* = 200$ N. (c) Sequence of four deformed configurations of the frame's centroidal axis attained for different load values, highlighting the occurrence of lateral buckling. (d) Convergence behavior of the various 3D beam virtual elements implemented. Plots of the relative error $\epsilon_w$ of the out-of-plane displacement component of the loaded point under a force value of 84 N vs. the mesh refinement level.

### 4.3. *Lateral buckling of a cantilever right-angle frame*

A second case study involving buckling is here presented. Previously analyzed by Argyris et al. [47], Simo and Vu-Quoc [15], and da Costa e Silva et al. [48], a right-angle frame with equal length $L$ of the two beams is fixed at one end (see Fig. 4). The corresponding material and geometrical data are set according to [15,47], and are reported in Fig. 4(a), where the high slenderness of the rectangular cross section can be observed. The free end is loaded with an in-plane transversal force $F_x$, having a final value $F_x^* = 2.5$ N, as well as with a perturbation force $F_z = F_x/1000$ acting along the out-of-plane direction $\boldsymbol{e}_3$, driving the structure to the buckling mode. After performing a preliminary convergence analysis similar to the previous benchmark test (see Section 4.2), each leg of the L-shaped frame has been discretized with $10^3$ VEB-2T elements.

The full equilibrium path, characterized in terms of the transverse end load $F_x$ versus the out-of-plane displacement component $w$, has been computed employing the arc-length continuation method. For consistency, both quantities have been normalized, taking as references the value $F_0 = 1$ N for $F_x$ and the beam length $L$ for $w$. The computed buckling transverse load was found to be $F_{x,\mathrm{cr}} \simeq 1.088$ N, which is in very good agreement with other values reported in earlier studies [15,47]. The load-displacement curve obtained from the present model is shown in Fig. 4(b) (solid colored line) and is compared against the solution previously determined by Argyris et al. [47] (dashed black line). Excellent agreement is observed between the two approaches, as the curves perfectly overlap for load levels up to the critical load $F_{x,\mathrm{cr}}$. The very slight discrepancy occurring for load values greater than the buckling load can be attributed to the fact that the lateral perturbation force was not removed during our simulation, unlike the approaches of previous researchers [15,47]. Finally, Fig. 4(c) shows a 3D view of the deformed configurations of the centroidal line, corresponding to three representative values of the transverse end load $F_x$: the buckling load $F_{x,\mathrm{cr}}$, the final load $F_x^*$, and an intermediate load of approximately 1.585 N.

### 4.4. *Bending of a cantilever beam to a closed circle and to a helical beam*

This benchmark example is inspired by the works of Simo and Ibrahimbegovic [15,21] and is introduced to test the proposed VE formulation in the presence of very large displacements and rotations. It involves an initially straight cantilever beam having length

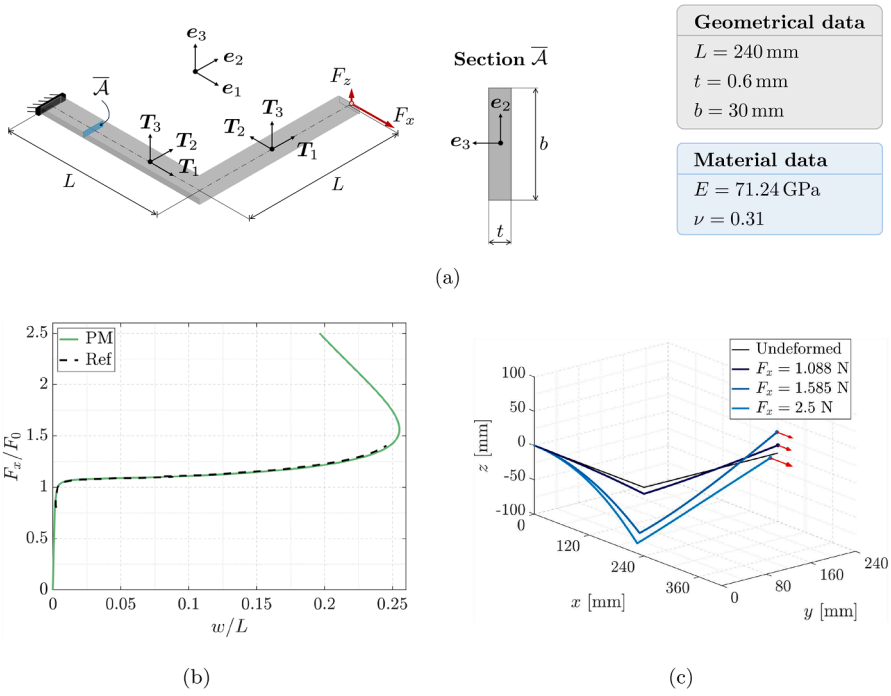


**Fig. 4.** Lateral buckling of a cantilever right-angle frame. (a) Problem description and notation. (b) Complete equilibrium path of the dimensionless out-of-plane displacement component $w/L$ of the tip under an applied in-plane force $F_x$ with final value $F_x^* = 2.5\,\text{N}$. The solid and dashed lines correspond to the numerical solution computed with the present model (PM), and to the reference solution (Ref) obtained by Argyris et al. [47]. (c) Deformed configurations for three subsequent values of the transverse end load $F_x$, highlighting the occurrence of lateral buckling of the frame.

$L = 100\,\text{mm}$ and a circular cross section of radius $r = 0.2\,\text{mm}$. Two different final configurations have been considered: pure bending into a closed circular arc and coiling into a helical shape.

As depicted in Fig. 5(a), in the first case, the straight rod is clamped at one end and subjected to an out-of-plane (i.e., along the $\boldsymbol{e}_3$ direction) concentrated moment $M$ applied at its free end. The Poisson's ratio and Young's modulus of the material are set respectively to 0 and 80 GPa. Under these assumptions, the exact solution to this problem corresponds to a deformed configuration consisting of a circular arc with radius $\rho = EI/M$, leading to the following analytical expressions for the tip rotation $\psi_{\text{L}}$ and the horizontal and vertical displacement components $u_{\text{L}}$ and $v_{\text{L}}$ of the free end:

$$\psi_{\text{L}} = \frac{ML}{EI}, \tag{44}$$

$$u_{\text{L}} = L\left(\frac{\sin\psi_{\text{L}}}{\psi_{\text{L}}} - 1\right), \tag{45}$$

$$v_{\text{L}} = L\left(\frac{1-\cos\psi_{\text{L}}}{\psi_{\text{L}}}\right). \tag{46}$$

A particularly significant case occurs when a moment $M_1 = 2\pi EI/L$ is imposed, for which the deformed configuration of the rod corresponds to a complete closed circle. In this test, a concentrated moment $M^* = 5M_1 = 10\pi EI/L$ has been applied along the $\boldsymbol{e}_3$ direction, causing the rod to coil around itself five times.

The problem has been treated numerically using the proposed 3D beam virtual element framework. Specifically, the rod has been discretized with $10^2$ VEB-2T elements, and the nonlinear equilibrium path has been determined by means of the arc-length method. The displacement components of the free end, normalized by the total length of the beam, are plotted in Fig. 5(b) as functions of the load multiplier $\lambda = M/M_1$. It is possible to note the almost exact correspondence between the numerical predictions (PM curves) and the reference theoretical solution given by Eqs. (45) and (46) (Ref curves), further validating the consistency and accuracy of the proposed approach. This evidence is also substantiated by the analysis of the deformed configurations assumed by the rod. The sequence of deformed shapes shown in Fig. 5(c), corresponding to positive integer values of the load multiplier (i.e. $\lambda = 1, 2, \ldots, 5$), clearly illustrates the expected coiling behavior, as the rod progressively bends into circular loops with increasing curvature.

After validating the proposed VE formulation in a two-dimensional framework through a comparison between the numerical results obtained and the theoretical solution, a modified three-dimensional version of this benchmark, introduced by [21] and later addressed also by [11], has been considered. In this three-dimensional setting, the same cantilever is bent to a helical shape by simultaneously applying at the free end a concentrated moment $M$ and a concentrated force $F$ having final values $M^* = 5M_1 = 10\pi EI/L$ and

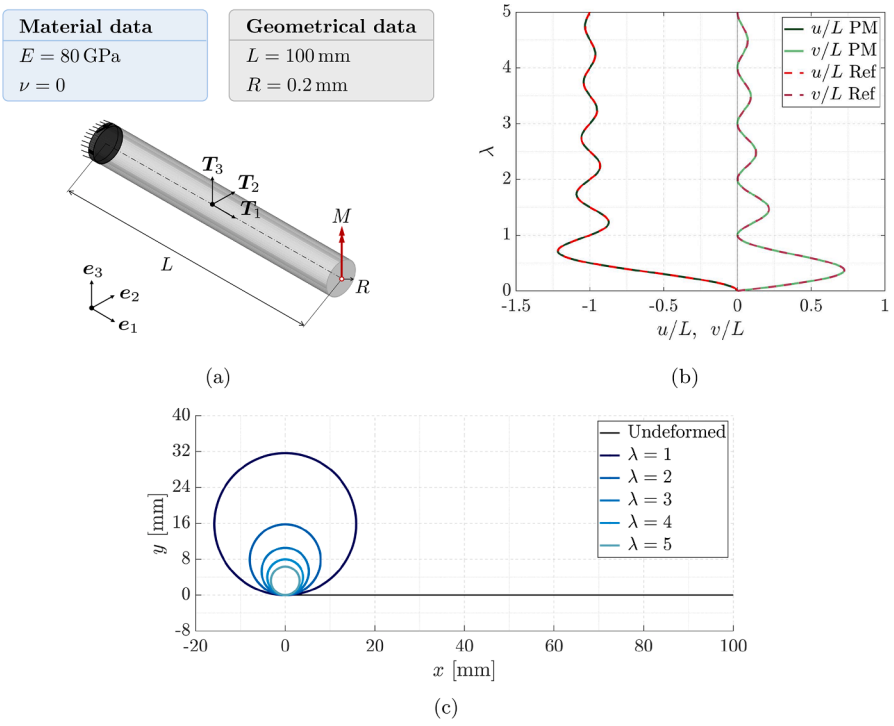


**Fig. 5.** Pure bending of an initially straight beam. (a) Problem description and notation. (b) Equilibrium path of the dimensionless in-plane displacement components $u/L$, $v/L$ of the free end under an applied out-of-plane concentrated moment $M$ with final value $M^* = 5M_1 = 10\pi EI/L$. The solid and dashed lines (actually, overlapping almost exactly) correspond to the numerical solution computed with the present model (PM), and to the reference analytical solution (Ref) given by Eqs. (45)-(46), respectively. (c) Subsequent deformed configurations of the rod under the applied moment values $\lambda M_1$, with $\lambda = 1, 2, \ldots, 5$.

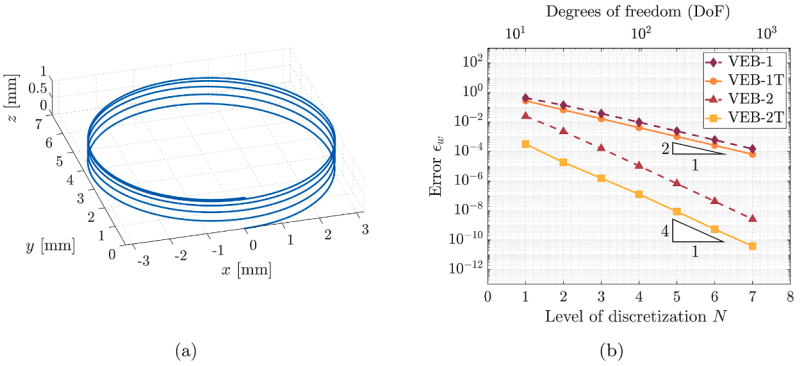


**Fig. 6.** Coiling of an initially straight beam into a helical shape. (a) Deformed configuration under an applied out-of-plane concentrated force $F^* = 0.01\,\mathrm{N}$ and moment $M^* = 5M_1 = 10\pi EI/L$. (b) Convergence behavior of the different 3D beam virtual elements implemented. Plots of the relative error $\epsilon_v$ of the in-plane displacement component $v$ of the free end (attained for $\lambda = 1/2$) vs. the mesh refinement level.

$F^* = 0.01\,\mathrm{N}$, respectively, and both acting along the $e_3$ axis. The beam has been discretized using $10^2$ VEB-2T elements, and the arc-length method has been employed to trace the full equilibrium path of the loaded free end. Note that in this case, the load multiplier $\lambda$ refers to both force and moment applied at the free end. The final shape of the beam, shown in Fig. 6(a), is consistent with the one previously obtained by other researchers [11,21]. This further confirms the accuracy of the proposed VE approach and highlights the ability of the proposed framework to effectively capture structural responses under challenging loading conditions and three-dimensional large rotation and deflection regimes.

Finally, similarly to the previous examples, a convergence study has been conducted in this three-dimensional setting to assess the performance of the four virtual elements developed. To this end, a value $\lambda = 1/2$ of the loading condition multiplier has been selected. The corresponding out-of-plane displacement of the free end $w_r$, selected as a reference for this analysis, has been numerically obtained employing a fine discretization consisting of $10^3$ VEB-2T elements. A set of 7 meshes with increasing refinement levels have been

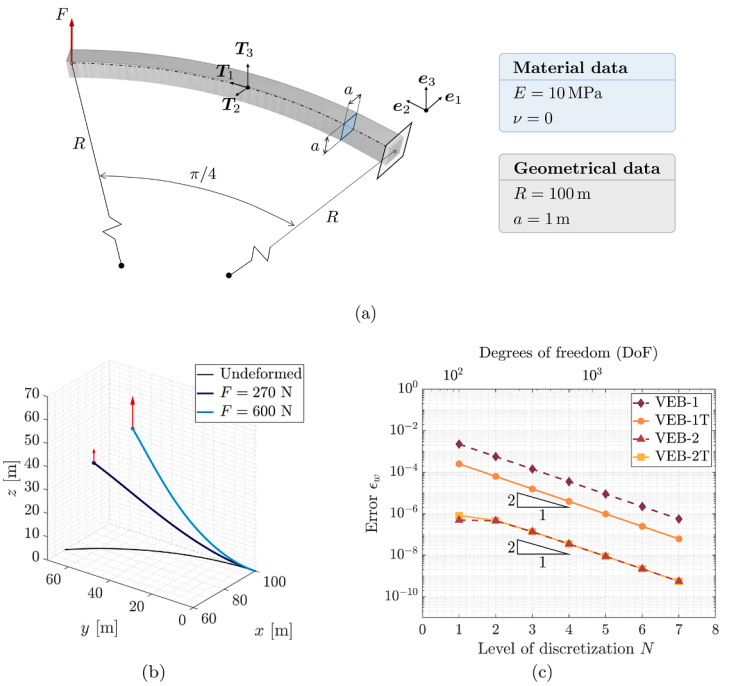


**Fig. 7.** Bathe's curved cantilever. (a) Problem description and notation. (b) Deformed configurations of the cantilever under different values of the force at the tip. (c) Convergence rates for the VEB-1, VEB-1T, VEB-2 and VEB-2T elements: relative error $\epsilon_w$ of the vertical displacement component $w$, under an applied force $F^* = 600\,\mathrm{N}$, vs. the mesh refinement level.

defined, where the $N$th mesh (with $N \in \{1, 2, \dots, 7\}$) stands for a discretization consisting of $2^{N-1}$ beam virtual elements and $12 \cdot 2^{N-1}$ DoFs. For each discretization level, the relative error $\epsilon_w = |w_N - w_\mathrm{r}|/w_\mathrm{r}$ between the vertical displacement component of the free end $w_N$ obtained from the $N$th numerical solution and its reference value $w_\mathrm{r}$ has been computed. The convergence behavior, shown in Fig. 6(b), highlights the superior performance of higher-order elements. Notably, both VEB-2 and especially VEB-2T elements achieve very accurate results with as few as one virtual element, whereas lower-order elements require significantly finer discretizations to attain comparable accuracy. While maintaining the same order of convergence rate, the VEB-2T element has a considerably higher accuracy (see Fig. 6), which relates to the importance of the torsional deformation on the solution.

### 4.5. Bathe's curved cantilever

We now investigate the performance of the proposed VE formulation for a beam with an initial curvature in the reference configuration. This benchmark test concerns a widely studied three-dimensional cantilever beam problem, originally introduced by Bathe and Bolourchi [49] and subsequently investigated also by other researchers (see, e.g., [11,15,18,19]). As depicted in Fig. 7(a), the beam, whose axis is a 45-degree circular arc with radius $R = 100\,\mathrm{m}$ in the undeformed configuration, is clamped at one end and subjected to a vertical point force $F$ at the free end, with a final magnitude $F^* = 600\,\mathrm{N}$. The material and section properties have been set in agreement with the aforementioned studies and are summarized in Fig. 7(a).

To allow a direct and consistent comparison with previous studies, in a first numerical simulation, the beam has been discretized using eight VEB-2T elements, thus matching the number of elements employed by [11,15,18,19,49]. The external load has been applied incrementally at the tip, considering a maximum value for the load increment equal to $\Delta F = F^*/20$. The displacement components of the tip obtained with the proposed VE formulation align well with the other existing solutions, as can be seen from the numerical values reported in Table 1. Fig. 7(b) shows two representative deformed configurations assumed by the initially curved cantilever in this loading scenario, achieved for the final load value and for an intermediate force value equal to 270 N.

A mesh convergence study is then carried out to further assess the performance of the proposed VE formulation. The purpose is to investigate how the discretization influences the numerical estimate of the vertical displacement component $w$ under the value $F^*$ of the applied force. Since no closed-form solution is available for this problem, the reference solution (the "converged" solution) has been defined as the one obtained by discretizing the curved cantilever with $10^4$ VEB-2T elements, leading to the values reported in the last row of Table 1. This convergence study has been performed through a series of 7 meshes, where the $N$th mesh (with $N \in \{1, 2, \dots, 7\}$) consists of $10 \cdot 2^{N-1}$ virtual elements. For the $N$th discretization level, the vertical displacement component of the tip $w_N$ has been computed. The corresponding relative error has been defined as $\epsilon_w = |w_N - w_\mathrm{r}|/w_\mathrm{r}$, adopted as the primary metric for quantifying the convergence rate. The convergence behavior of the various virtual elements implemented is shown in Fig. 7(c). Interestingly, it is observed that for the curved cantilever the two higher-order elements (VEB-2 and VEB-2T) exhibit essentially identical convergence

**Table 1**
Bathe's curved cantilever. Comparison of the free end displacement components against reference results obtained in previous works (N.A.: data not available).

| 8 elements | | | |
|---|---|---|---|
| $u$ [m] | $v$ [m] | $w$ [m] | Reference |
| 13.55 | 23.56 | 53.43 | Present formulation (VEB-2T) |
| 13.50 | 23.48 | 53.37 | Simo and Vu-Quoc [15] |
| 13.39 | 23.51 | 53.40 | Bathe and Bolourchi [49] |
| 13.68 | 23.87 | 53.71 | Crisfield [19] |
| 13.74 | 23.67 | 53.50 | Cardona and Geradin [18] |
| N.A. | N.A. | 53.47 | Magisano et al. [11] |
| $10^4$ elements | | | |
| 13.60 | 23.56 | 53.47 | Present formulation (VEB-2T) |

rates as the lower-order elements (VEB-1 and VEB-1T), regardless of the ansatz adopted for the axial component of the Euler rotation vector. Hence, for initially curved beams, the proposed framework is associated with a suboptimal convergence rate for the VEs based on a higher-order ansatz. This degradation in convergence performance somehow resembles the behavior also observed in the VE approximation of two- or three-dimensional domains with curved and regular boundaries [50,51]. For instance, in [51] was in fact demonstrated that the error introduced by approximating a curved edge with a piecewise linear one leads to a suboptimal convergence rate. Similarly, a possible explanation for the suboptimal rate in this context is that, while lower-order elements do not suffer in terms of convergence rate, since the geometry approximation introduces an error of the same order as that related to the interpolation scheme of rotations and displacements, for higher-order elements the geometric approximation error becomes dominant. Therefore, increasing the order of the elements is unlikely to yield improved convergence rates. This conjecture is further corroborated by the two-dimensional numerical experiment presented in the following subsection. However, note that the error related to the results of VEB-2 and VEB-2T is two orders of magnitude smaller than for the elements VEB-1 and VEB-1T.

### 4.6. Clamped-hinged deep circular arc subjected to a point load

To investigate if the suboptimal convergence properties highlighted in Section 4.5 are due to either the geometric approximation error or the 3D nature of the case study, we now address a 2D benchmark test, previously investigated, e.g., by [15,52,53]. This example considers a beam whose line of centroids in the reference configuration forms a circular arc of radius $R = 100\,\text{m}$ subtending an angle $2\alpha = 215°$ (see Fig. 8(a)). The arc is clamped at one end, hinged at the other, and subjected to a downward point load $F$ applied at the crown. The beam is made of a linear elastic material with $E = 10\,\text{MPa}$ and Poisson coefficient $\nu = 0$. It has a square cross section of side length $a = 1\,\text{m}$ (from which the geometric parameters follow: $I_2 = I_3 = 1/12\,\text{m}^4$, $\chi_2 = \chi_3 = 6/5$, $J_t = 2I_2$).

As the applied load is progressively increased, the arc undergoes large deflections and eventually, for a value of the point load equal to $F_{\text{cr}}$, reaches a critical point beyond which instability occurs. For this problem, DaDeppo and Schmidt [54] provided an exact solution for $F_{\text{cr}}$, for the critical horizontal and vertical displacements at the crown $u_{\text{cr}}$ and $v_{\text{cr}}$, as well as for the critical rotation of the cross section at the crown $\beta_{\text{cr}}$. Based on the geometric and material data defined earlier, the following values for the critical values are obtained: $F_{\text{cr}} = 747.50\,\text{N}$, $-u_{\text{cr}}/R = 0.6116$, $-v_{\text{cr}}/R = 1.1372$, $\beta_{\text{cr}} = 0.0498\,\text{rad}$.

In a first simulation, the problem has been numerically addressed by discretizing the circular arc with $10^3$ VEB-2T elements, and a maximum applied load of $F^* = 800\,\text{N}$ has been prescribed to capture the full nonlinear response of the structure, including the post-buckling regime. Considering this value of the applied force, the resulting equilibrium paths for the normalized horizontal and vertical displacement components of the crown, $-u/R$ and $-v/R$, are reported in Fig. 8(b). Furthermore, Fig. 8(c) depicts five subsequent representative deformed configurations assumed by the arc during the loading path. In this case, the numerical simulation yields the following values for the critical load, and for the critical displacements and rotation of the crown: $F_{\text{cr,num}} = 747.56\,\text{N}$, $-u_{\text{cr,num}}/R = 0.6115$, $-v_{\text{cr,num}}/R = 1.1373$, and $\beta_{\text{cr,num}} = 0.0498\,\text{rad}$, which are in very good agreement with the analytical predictions.

After determining the complete equilibrium path, a force value slightly lower than the critical load (equal to $745\,\text{N}$) has been selected to perform a convergence study, similar to the previous examples. In this case, the objective is to assess the impact of the discretization on the vertical displacement at the crown for the chosen force value. The reference numerical solution has been computed using a highly refined mesh comprising $10^5$ VEB-2T elements, for which the value $v_{\text{r}} = -111.754\,\text{m}$ has been obtained. Eight different discretization levels have been defined for this convergence study, where the $N$th mesh (with $N \in \{1, 2, \dots, 8\}$) consists of $10 \cdot 2^N$ elements and $120 \cdot 2^N$ DoF. The results of this convergence analysis, again given in terms of relative error $\epsilon_v = |v_N - v_{\text{r}}|/v_{\text{r}}$, are reported in Fig. 8(d). It is noteworthy that, as observed in the previous example (see Section 4.5), the convergence rates associated with all VE formulations are essentially identical. These findings further validate the robustness and general effectiveness of the proposed VE framework for geometrically exact 3D beam formulations. However, they also seem to confirm the need for more refined formulations when curved beams are considered in order to restore the desired optimal convergence rate in curved geometries.

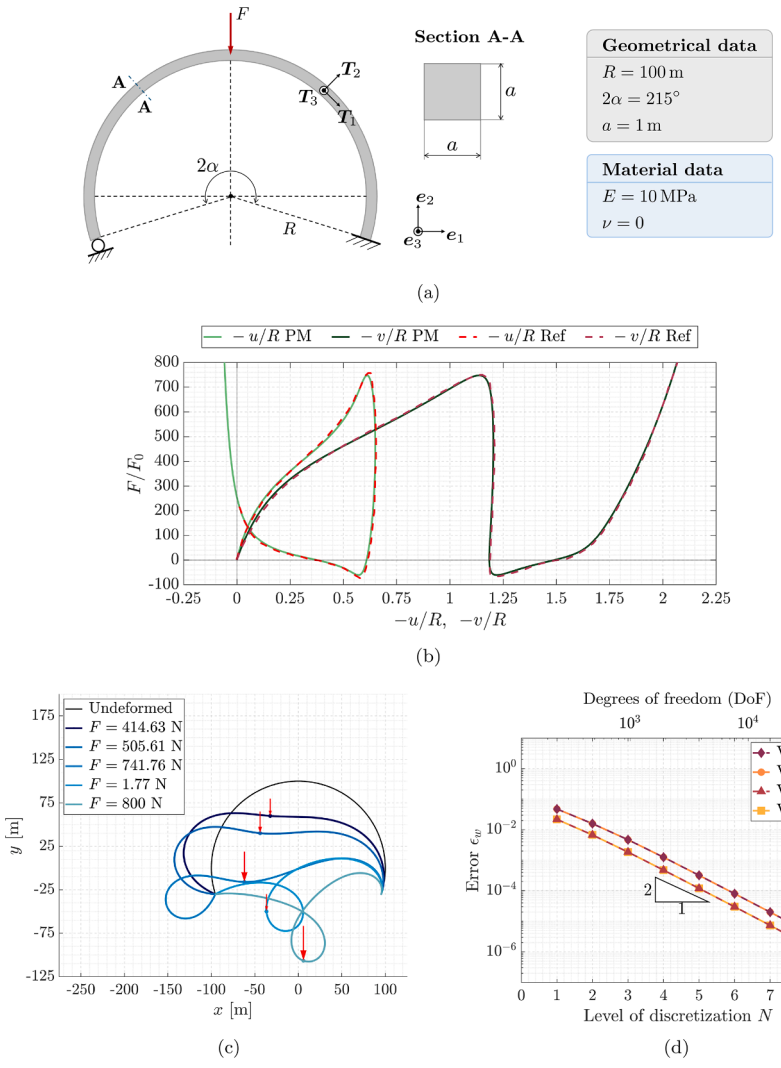


**Fig. 8.** Clamped-hinged deep circular arc subjected to a point load. (a) Problem description. (b) Equilibrium paths of the normalized horizontal and vertical displacement components of the crown for a maximum force value $F^* = 800\,\text{N}$. The reference (Ref) curves have been extracted from [15]. (c) Five illustrative deformed configurations. (d) Convergence rates of the four VE implemented. Relative error $\epsilon_v$ of the vertical displacement component of the crown corresponding to an applied force 745 N vs. the mesh refinement level.

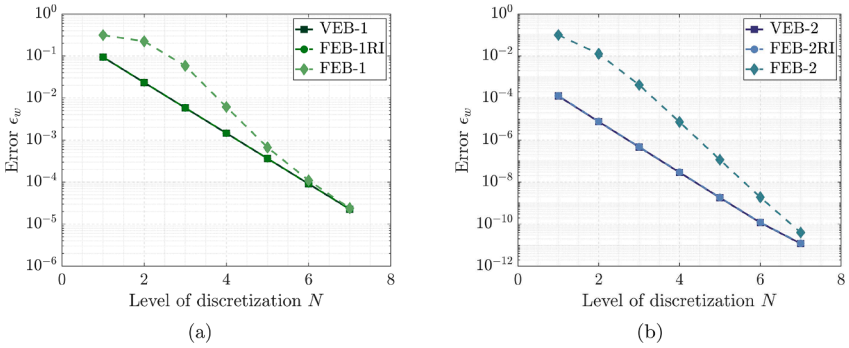


**Fig. 9.** Convergence behavior of 3D nonlinear beam elements based on VE and FE numerical schemes for the case of Crisfield's L-shaped cantilever (see Section 4.1). Plots of the relative error $\epsilon_w$ of the vertical displacement component $w$ of the tip under a force value $F^* = 5\,\text{N}$ vs. the mesh refinement level. (a) Beam elements based on a linear ansatz for rotations and quadratic ansatz for displacements. (b) Beam elements based on a quadratic ansatz for rotations and cubic ansatz for displacements.

### 4.7. Comparison between VE- and FE-based numerical schemes

In this section we briefly present a numerical comparison between the proposed VE formulation for 3D beams and discretization schemes based on the FE method, with the aim of highlighting possible similarities between the two approaches. The comparison is shown in terms of convergence behavior for the considered discretization schemes and refers to the numerical application of the Crisfield's L-shaped cantilever (see Section 4.1). Specifically, the convergence rate of the virtual element VEB-1 is compared with those of two finite elements, denoted as FEB-1 and FEB-1RI, which have been implemented through in-house codes with AceGen. The FEB-1 element employs a linear polynomial approximation for the rotation components and a quadratic approximation for the displacement components. The FEB-1RI element adopts the same interpolation ansatz as FEB-1 but additionally incorporates a reduced integration technique. An analogous comparison has been carried out for higher-order schemes: the convergence performance of the VEB-2 element is compared with that of the two finite elements, FEB-2 and FEB-2RI, which are both based on a quadratic approximation for rotations and a cubic approximation for displacements, with the only difference that the FEB-2RI element incorporates reduced integration. Note that, differently from the VE approach, all the elements built using FE concepts employ classical Lagrangian polynomials as shape functions (so, they involve a mapping from the parent space to the physical space), as well as additional nodes if quadratic and/or cubic interpolations are considered. It is also worth remarking that, to the best of the authors' knowledge, FE-based numerical formulations involving a quadratic/cubic Lagrangian interpolation ansatz for 3D beams in the nonlinear regime are not available in the literature.

The numerical results of the convergence tests are reported in Fig. 9(a) and (b), which show the plots of the relative error $\epsilon_w$, computed as described in Section 4.1, for the VE- and FE-based schemes using the linear/quadratic and quadratic/cubic interpolation ansatz, respectively. In both cases, the results indicate that the proposed VE formulation exhibits the same locking-free behavior and optimal convergence rates observed for finite elements employing reduced integration. Conversely, when a "standard" FE implementation (i.e., without resorting to special techniques such as reduced integration) is used, both these aspects are lost. These findings therefore suggest that the proposed VE approach for nonlinear 3D beams is equivalent, in terms of numerical performance, to a nonstandard FEM that employs reduced integration strategies, thus generalizing to the nonlinear 3D context the result shown by Wriggers in the 2D linear case [27,40]. However, the VE framework achieves these desirable properties in a conceptually simpler, more modular, and more straightforward manner, which facilitates the construction of high-order, locking-free 3D beam elements in the geometrically nonlinear regime compared to their FE-based counterparts.

## 5. Conclusion

In this work, a novel numerical approach based on the VE method has been developed for the analysis of geometrically exact 3D shear-deformable beams undergoing large displacements and finite rotations. The proposed approach enables the automatic construction of new one-dimensional virtual elements of arbitrary order, achieving flexibility and convergence properties which, to the best of the authors' knowledge, are not obtainable with existing FE-based formulations without relying on tailored enhancements or ad hoc treatments in sophisticated approaches [55]. The internal variables (moments) that arise when considering higher-order ansatz functions are condensed element-wise. As a result, only the nodal degrees of freedom, located at the element endpoints, enter the formulation, making these new virtual elements straightforward to implement within standard FE codes.

The consistency and effectiveness of the proposed formulation have been assessed through a series of well-established numerical benchmarks that involve beams, frames, and structures subjected to large deflections and rotations. In these applications, virtual elements based on linear/quadratic and quadratic/cubic interpolations have been considered. Specifically, VEB-$n$ elements (with $n = 1, 2$) have been constructed assuming a polynomial ansatz of degree $n$ for the rotations and $n + 1$ for the displacements. On the other hand, VEB-$n$T elements (with $n = 1, 2$) are based on a polynomial ansatz of order $n + 1$ for both the displacements and the axial rotation, and of order $n$ otherwise. The results clearly demonstrate that the developed 3D beam virtual elements are robust, locking-free, and highly accurate, particularly for initially straight beam geometries and if high-order ansatz functions are employed. In some cases, the VEB-$n$T formulation yields lower absolute errors compared to the corresponding VEB-$n$ formulation, although both types of virtual elements exhibit the same convergence rate. However, since this improvement is not systematic across all cases, further investigation would be beneficial and will be conducted in future studies.

For beams with an initial curvature, the proposed framework leads to a suboptimal convergence rate upon mesh refinement for high-order ansatz functions. This behavior is likely due to the error introduced by approximating an initially curved geometry with straight elements. To address this limitation, a promising strategy could be generalizing the present approach by defining new curved one-dimensional virtual elements. Such an extension would require a revised definition of the projection operator and is planned to be part of the ongoing development of the VE-based numerical framework presented here.

## CRediT authorship contribution statement

**Pierfrancesco Gaziano:** Writing – review & editing, Writing – original draft, Visualization, Validation, Software, Resources, Methodology, Investigation, Formal analysis, Data curation, Conceptualization; **Michele Marino:** Writing – review & editing, Validation, Supervision, Resources, Project administration, Methodology, Investigation, Funding acquisition, Formal analysis, Conceptualization; **Giuseppe Vairo:** Writing – review & editing, Validation, Supervision, Resources, Project administration, Investigation, Funding acquisition, Formal analysis; **Peter Wriggers:** Writing – review & editing, Validation, Supervision, Software, Resources, Project administration, Methodology, Investigation, Funding acquisition, Formal analysis, Data curation, Conceptualization.

## Data availability

Data will be made available on request.

## Declaration of competing interest

The authors declare that they have no known competing financial interests or personal relationships that could have appeared to influence the work reported in this paper.

## Acknowledgments

Part of this work was carried out with the support from the Italian National Group for Mathematical Physics GNFM-INdAM. Pierfrancesco Gaziano and Giuseppe Vairo acknowledge financial support by the Italian Ministry of University and Research (MUR) under the National Recovery and Resilience Plan (NRRP), PRIN 2022 program, Project 2022T3SLAZ – CUP E53D23003700006. Michele Marino acknowledges financial support under the National Recovery and Resilience Plan (NRRP) by the Italian Ministry of University and Research (MUR), funded by the European Union - NextGenerationEU, within the PRIN 2022 program, Project 2022Z24WLR (project acronym: MATERIAL), CUP: E53C24002920006.

## Appendix A.

Here we prove that $c_0 = p_1$ for a generic polynomial ansatz, generalizing the result obtained by Wriggers in some special cases [40]. The constant part of the projection, $c_0$, can be computed from Eq. (20), which essentially states that the average value of the approximation $p_h$ of the primary variable in $\Omega_e$ must be equal to the average of its consistent part $p_\pi^{(n)}$. The following two cases are possible.

(a) Linear ansatz ($n = 1$). In this case, the condition given in Eq. (20) can be substituted by the following [39]:

$$\frac{1}{2}\sum_{i=1}^{2} p_\pi^{(1)}(\xi_i) = \frac{1}{2}\sum_{i=1}^{2} p_h(\xi_i), \tag{A.1}$$

where $\xi_1 = 0$ and $\xi_2 = l_e$ are the local coordinates of the two element endpoints. Since the function $p_h$ is known only at the element nodes by definition, substituting in Eq. (A.1) the linear polynomial ansatz given in Eq. (23) yields:

$$2c_0 + l_e\, c_1 = p_1 + p_2. \tag{A.2}$$

Inserting the expression $c_1 = \frac{p_2 - p_1}{l_e}$ obtained from Eqs. (29), (A.2) is recast into:

$$2c_0 + p_2 - p_1 = p_1 + p_2, \tag{A.3}$$

from which clearly follows that $c_0 = p_1$.

(b) Higher-order ansatz ($n \geq 2$). In this case, the right-hand side of Eq. (20) is related to the moment $m_{(p),0}$ through Eq. (22):

$$\int_0^{l_e} p_h \,\mathrm{d}\xi = m_{(p),0}\, l_e. \tag{A.4}$$

Recalling Eqs. (23) and (29), the left-hand side of Eq. (20) can instead be written as:

$$\int_0^{l_e} p_\pi^{(n)} \,\mathrm{d}\xi = \int_0^{l_e} \left(c_0 + \mathsf{N}_\pi^{(n)\mathrm{T}}\hat{\mathsf{c}}\right) \mathrm{d}\xi = c_0\, l_e + \mathsf{M}^{(n)\mathrm{T}}\mathsf{H}\,\mathsf{p}_e^{(n)}, \tag{A.5}$$

where $\mathsf{M}^{(n)}$ is defined as $\mathsf{M}^{(n)} = \int_0^{l_e} \mathsf{N}_\pi^{(n)} \,\mathrm{d}\xi = \left[\frac{l_e^2}{2}, \frac{l_e^3}{3}, \ldots, \frac{l_e^{n+1}}{n+1}\right]^{\mathrm{T}}$. Equating Eqs. (A.4) and (A.5) after substituting the relationship $\mathsf{H} = \mathsf{G}^{-1}\,\mathsf{A}$ in Eq. (A.5) yields:

$$m_{(p),0} = c_0 + \frac{1}{l_e}\,\mathsf{Q}^{(n)\mathrm{T}}\,\mathsf{A}\,\mathsf{p}_e^{(n)}, \tag{A.6}$$

where by definition $\mathsf{Q}^{(n)\mathrm{T}} = \mathsf{M}^{(n)\mathrm{T}}\,\mathsf{G}^{-1}$.

To obtain an explicit form of the vector $\mathsf{Q}^{(n)}$, observe that the element $(i, j)$ of the matrix $\mathsf{G}$ can be written in closed form as:

$$\mathsf{G}_{ij} = \int_0^{l_e} \mathsf{B}_{\pi,i}^{(n)}\,\mathsf{B}_{\pi,j}^{(n)} \,\mathrm{d}\xi = i\,j\,\frac{l_e^{i+j-1}}{i+j-1}, \qquad 1 \leq i, j \leq n. \tag{A.7}$$

Now, it can be verified that the $j$th component of $\mathsf{M}^{(n)}$, $\mathsf{M}_j^{(n)}$, is given by:

$$\mathsf{M}_j^{(n)} = \frac{l_e^{j+1}}{j+1} = l_e\,\mathsf{G}_{1j} - \frac{1}{2}\,\mathsf{G}_{2j}, \qquad 1 \leq j \leq n. \tag{A.8}$$

Then, from the previous condition it follows that $\mathsf{Q}_j^{(n)} = 0\ \forall j \geq 3$ (with $j \leq n$), since the quantities $\mathsf{M}_j^{(n)}$ are expressed exactly as a linear combination of the first two row vectors of $\mathsf{G}$, $\mathsf{G}_{1j}$ and $\mathsf{G}_{2j}$. Hence, it results:

$$\mathsf{Q}^{(n)\mathrm{T}} = \begin{bmatrix} l_e & -\frac{1}{2} & \mathbf{0}_{1\times(n-2)} \end{bmatrix}, \tag{A.9}$$

from which, recalling Eq. (28), it follows:

$$\mathsf{Q}^{(n)\mathrm{T}}\,\mathsf{A} = \begin{bmatrix} -l_e & 0 & l_e & 0 & \dots & 0 \end{bmatrix}. \tag{A.10}$$

Substitution of Eqs. (A.10) in (A.6) finally yields:

$$m_{(p),0} = c_0 - \begin{bmatrix} 1 & 0 & -1 & 0 & \dots & 0 \end{bmatrix} \mathsf{p}_e^{(n)} = c_0 - p_1 + m_{(p),0}, \tag{A.11}$$

which proves the proposition.

## References


[1] D.H. Hodges, Nonlinear Composite Beam Theory, American Institute of Aeronautics and Astronautics, 2006. https://doi.org/10.2514/4.866821

[2] E. Oñate, Structural Analysis With The Finite Element Method. Linear Statics: Volume 2: Beams, Plates and Shells, Springer Science & Business Media, 2013. https://doi.org/10.1007/978-1-4020-8743-1

[3] A. Sabale, K.V.N. Gopal, Nonlinear aeroelastic response of wind turbines using Simo-Vu-Quoc rods, Appl. Math. Model. 65 (2019) 696–716. https://doi.org/10.1016/j.apm.2018.09.003

[4] C. Meier, W.A. Wall, A. Popp, A unified approach for beam-to-beam contact, Comput. Methods Appl. Mech. Eng. 315 (2017) 972–1010. https://doi.org/10.1016/j.cma.2016.11.028

[5] C. Meier, M.J. Grill, W.A. Wall, A. Popp, Geometrically exact beam elements and smooth contact schemes for the modeling of fiber-based materials and structures, Int. J. Solids Struct. 154 (2018) 124–146. https://doi.org/10.1016/j.ijsolstr.2017.07.020

[6] C.J.F. Júnior, A.C.P. Cardozo, V.M. Júnior, A.G. Neto, Modeling wind turbine blades by geometrically-exact beam and shell elements: a comparative approach, Eng. Struct. 180 (2019) 357–378. https://doi.org/10.1016/j.engstruct.2018.09.032

[7] X. Ma, N. An, Q. Cong, J.-B. Bai, M. Wu, et al., Design, modeling, and manufacturing of high strain composites for space deployable structures, Commun. Eng. 3 (1) (2024) 78. https://doi.org/10.1038/s44172-024-00223-2

[8] T.-W. Liu, J.-B. Bai, N. Fantuzzi, X. Zhang, Thin-walled deployable composite structures: a review, Prog. Aerosp. Sci. 146 (2024) 100985. https://doi.org/10.1016/j.paerosci.2024.100985

[9] N. San Ha, G. Lu, A review of recent research on bio-inspired structures and materials for energy absorption applications, Compos. Part B: Eng. 181 (2020) 107496. https://doi.org/10.1016/j.compositesb.2019.107496

[10] P. Gaziano, L. Zoboli, E. Monaldo, G. Vairo, Effective mechanical response of biomimetic staggered composites: closed-form estimates via a micromechanical variational formulation, J. Mech. Phys. Solids 200 (2025) 106137. https://doi.org/10.1016/j.jmps.2025.106137

[11] D. Magisano, L. Leonetti, G. Garcea, Isogeometric analysis of 3D beams for arbitrarily large rotations: locking-free and path-independent solution without displacement DOFs inside the patch, Comput. Methods Appl. Mech. Eng. 373 (2021) 113437. https://doi.org/10.1016/j.cma.2020.113437

[12] E. Reissner, On one-dimensional finite-strain beam theory: the plane problem, Zeitschrift für angewandte Mathematik und Physik ZAMP 23 (5) (1972) 795–804. https://doi.org/10.1007/BF01602645

[13] E. Reissner, On finite deformations of space-curved beams, Zeitschrift für angewandte Mathematik und Physik ZAMP 32 (6) (1981) 734–744. https://doi.org/10.1007/BF00946983

[14] J.C. Simo, A finite strain beam formulation. the three-dimensional dynamic problem. Part I, Comput. Methods Appl. Mech. Eng. 49 (1) (1985) 55–70. https://doi.org/10.1016/0045-7825(85)90050-7

[15] J.C. Simo, L. Vu-Quoc, A three-dimensional finite-strain rod model. Part II: computational aspects, Comput. Methods Appl. Mech. Eng. 58 (1) (1986) 79–116. https://doi.org/10.1016/0045-7825(86)90079-4

[16] A.A. Shabana, R.Y. Yakoub, Three dimensional absolute nodal coordinate formulation for beam elements: theory, J. Mech. Des. 123 (4) (2001) 606–613. https://doi.org/10.1115/1.1410100

[17] J. Frischkorn, S. Reese, A solid-beam finite element and non-linear constitutive modelling, Comput. Methods Appl. Mech. Eng. 265 (2013) 195–212. https://doi.org/10.1016/j.cma.2013.06.009

[18] A. Cardona, M. Géradin, A beam finite element non-linear theory with finite rotations, Int. J. Numer. Methods Eng. 26 (11) (1988) 2403–2438. https://doi.org/10.1002/nme.1620261105

[19] M.A. Crisfield, A consistent co-rotational formulation for non-linear, three-dimensional, beam-elements, Comput. Methods Appl. Mech. Eng. 81 (2) (1990) 131–150. https://doi.org/10.1016/0045-7825(90)90106-V

[20] C.A. Felippa, B. Haugen, A unified formulation of small-strain corotational finite elements: I. Theory, Comput. Methods Appl. Mech. Eng. 194 (21–24) (2005) 2285–2335. https://doi.org/10.1016/j.cma.2004.07.035

[21] A. Ibrahimbegovic, On the choice of finite rotation parameters, Comput. Methods Appl. Mech. Eng. 149 (1–4) (1997) 49–71. https://doi.org/10.1016/S0045-7825(97)00059-5

[22] F.S. Liguori, G. Zucco, A. Madeo, D. Magisano, L. Leonetti, G. Garcea, P.M. Weaver, Postbuckling optimisation of a variable angle tow composite wingbox using a multi-modal Koiter approach, Thin-Walled Struct. 138 (2019) 183–198. https://doi.org/10.1016/j.tws.2019.01.035

[23] B. Oesterle, R. Sachse, E. Ramm, M. Bischoff, Hierarchic isogeometric large rotation shell elements including linearized transverse shear parametrization, Comput. Methods Appl. Mech. Eng. 321 (2017) 383–405. https://doi.org/10.1016/j.cma.2017.03.031

[24] A. Ibrahimbegović, F. Frey, I. Kožar, Computational aspects of vector-like parametrization of three-dimensional finite rotations, Int. J. Numer. Methods Eng. 38 (21) (1995) 3653–3673. https://doi.org/10.1002/nme.1620382107

[25] P. Betsch, A. Menzel, E. Stein, On the parametrization of finite rotations in computational mechanics: a classification of concepts with application to smooth shells, Comput. Methods Appl. Mech. Eng. 155 (3–4) (1998) 273–305. https://doi.org/10.1016/S0045-7825(97)00158-8

[26] D. Magisano, L. Leonetti, A. Madeo, G. Garcea, A large rotation finite element analysis of 3D beams by incremental rotation vector and exact strain measure with all the desirable features, Comput. Methods Appl. Mech. Eng. 361 (2020) 112811. https://doi.org/10.1016/j.cma.2019.112811

[27] P. Wriggers, A locking free virtual element formulation for Timoshenko beams, Comput. Methods Appl. Mech. Eng. 417 (2023) 116234. https://doi.org/10.1016/j.cma.2023.116234

[28] I. Katili, Unified and integrated approach in a new Timoshenko beam element, Eur. J. Comput. Mech. 26 (3) (2017) 282–308. https://doi.org/10.1080/17797179.2017.1328643

[29] T.J.R. Hughes, R.L. Taylor, W. Kanoknukulchai, A simple and efficient finite element for plate bending, Int. J. Numer. Methods Eng. 11 (10) (1977) 1529–1543. https://doi.org/10.1002/nme.1620111005

[30] E.N. Dvorkin, K.-J. Bathe, A continuum mechanics based four-node shell element for general non-linear analysis, Eng. Comput. 1 (1) (1984) 77–88. https://doi.org/10.1108/eb023562

[31] K.-U. Bletzinger, M. Bischoff, E. Ramm, A unified approach for shear-locking-free triangular and rectangular shell finite elements, Comput. Struct. 75 (3) (2000) 321–334. https://doi.org/10.1016/S0045-7949(99)00140-6

[32] J. Kiendl, F. Auricchio, T.J.R. Hughes, A. Reali, Single-variable formulations and isogeometric discretizations for shear deformable beams, Comput. Methods Appl. Mech. Eng. 284 (2015) 988–1004. https://doi.org/10.1016/j.cma.2014.11.011
[33] F. Auricchio, L.B. Da Veiga, J. Kiendl, C. Lovadina, A. Reali, Locking-free isogeometric collocation methods for spatial Timoshenko rods, Comput. Methods Appl. Mech. Eng. 263 (2013) 113–126. https://doi.org/10.1016/j.cma.2013.03.009
[34] F. Auricchio, L.B. Da Veiga, T.J.R. Hughes, A. Reali, G. Sangalli, Isogeometric collocation methods, Math. Models Methods Appl. Sci. 20 (11) (2010) 2075–2107. https://doi.org/10.1142/S0218202510004878
[35] E. Marino, Isogeometric collocation for three-dimensional geometrically exact shear-deformable beams, Comput. Methods Appl. Mech. Eng. 307 (2016) 383–410. https://doi.org/10.1016/j.cma.2024.117283
[36] E. Marino, Locking-free isogeometric collocation formulation for three-dimensional geometrically exact shear-deformable beams with arbitrary initial curvature, Comput. Methods Appl. Mech. Eng. 324 (2017) 546–572. https://doi.org/10.1016/j.cma.2017.06.031
[37] G. Ferri, J. Kiendl, A. Reali, E. Marino, A fully explicit isogeometric collocation formulation for the dynamics of geometrically exact beams, Comput. Methods Appl. Mech. Eng. 431 (2024) 117283. https://doi.org/10.1016/j.cma.2024.117283
[38] L. Beirão Da Veiga, F. Brezzi, L.D. Marini, Virtual elements for linear elasticity problems, SIAM J. Numer. Anal. 51 (2) (2013) 794–812. https://doi.org/10.1137/120874746
[39] L. Beirão da Veiga, F. Brezzi, L.D. Marini, A. Russo, The Hitchhiker's guide to the virtual element method, Math. Models Methods Appl. Sci. 24 (08) (2014) 1541–1573. https://doi.org/10.1142/S021820251440003X
[40] P. Wriggers, On a virtual element formulation for trusses and beams, Arch. Appl. Mech. 92 (6) (2022) 1655–1678. https://doi.org/10.1007/s00419-022-02113-5
[41] A. Moallemi-Oreh, M. Karkon, Finite element formulation for stability and free vibration analysis of Timoshenko beam, Adv. Acoust. Vib. 2013 (1) (2013) 841215. https://doi.org/10.1155/2013/841215
[42] A. Ibrahimbegovic, R.L. Taylor, On the role of frame-invariance in structural mechanics models at finite rotations, Comput. Methods Appl. Mech. Eng. 191 (45) (2002) 5159–5176. https://doi.org/10.1016/S0045-7825(02)00442-5
[43] P. Wriggers, Nonlinear Finite Element Methods, Springer Science & Business Media, 2008.
[44] A.S. Petrolo, R. Casciaro, 3D beam element based on Saint Venànt's rod theory, Comput. Struct. 82 (29-30) (2004) 2471–2481. https://doi.org/10.1016/j.compstruc.2004.07.004
[45] J. Korelc, P. Wriggers, Automation of Finite Element Methods, Springer, 2016. https://doi.org/10.1007/978-3-319-39005-5
[46] G. Jelenić, M.A. Crisfield, Geometrically exact 3D beam theory: implementation of a strain-invariant finite element for statics and dynamics, Comput. Methods Appl. Mech. Eng. 171 (1-2) (1999) 141–171. https://doi.org/10.1016/S0045-7825(98)00249-7
[47] J.H. Argyris, H. Balmer, J.S. Doltsinis, P.C. Dunne, M. Haase, et al., Finite element method — the natural approach, Comput. Methods Appl. Mech. Eng. 17-18 (1979) 1–106. https://doi.org/10.1016/0045-7825(79)90083-5
[48] C. da Costa e Silva, S.F. Maassen, P.M. Pimenta, J. Schröder, A simple finite element for the geometrically exact analysis of Bernoulli–Euler rods, Comput. Mech. 65 (2020) 905–923. https://doi.org/10.1007/s00466-019-01800-5
[49] K.-J. Bathe, S. Bolourchi, Large displacement analysis of three-dimensional beam structures, Int. J. Numer. Methods Eng. 14 (7) (1979) 961–986. https://doi.org/10.1002/nme.1620140703
[50] L. Beirão da Veiga, A. Russo, G. Vacca, The virtual element method with curved edges, ESAIM: Math. Model. Numer. Anal. 53 (2) (2019) 375–404. https://doi.org/10.1051/m2an/2018052
[51] E. Artioli, L. Beirão da Veiga, F. Dassi, Curvilinear virtual elements for 2D solid mechanics applications, Comput. Methods Appl. Mech. Eng. 359 (2020) 112667. https://doi.org/10.1016/j.cma.2019.112667
[52] A.K. Noor, J.M. Peters, Mixed models and reduced/selective integration displacement models for nonlinear analysis of curved beams, Int. J. Numer. Methods Eng. 17 (4) (1981) 615–631. https://doi.org/10.1002/nme.1620170409
[53] P. Wriggers, J.C. Simo, A general procedure for the direct computation of turning and bifurcation points, Int. J. Numer. Methods Eng. 30 (1) (1990) 155–176. https://doi.org/10.1002/nme.1620300110
[54] D.A. DaDeppo, R. Schmidt, Instability of clamped-hinged circular arches subjected to a point load, J. Appl. Mech. 42 (4) (1975) 894–896. https://doi.org/10.1115/1.3423734
[55] C. Meier, A. Popp, W.A. Wall, Geometrically exact finite element formulations for slender beams: Kirchhoff–Love theory versus Simo–Reissner theory, Arch. Comput. Methods Eng. 26 (1) (2019) 163–243. https://doi.org/10.1007/s11831-017-9232-5